The Astrophysical Journal Supplement Series, 269:56 (17pp), 2023 December https://doi.org/10.3847/1538-4365/acfb03

Discovery and Timing of Millisecond Pulsars in the Globular Cluster M5 with FAST and Arecibo

Lei Zhang[1,2], Paulo C. C. Freire[3], Alessandro Ridolfi[3,4], Zhichen Pan[1,5,6,7], Jiaqi Zhao[8], Craig O. Heinke[8], Jianxing Chen[9,10], Mario Cadelano[9,10], Cristina Pallanca[9,10], Xian Hou[11,12,13], Xiaoting Fu[14,10], Shi Dai[1,15], Erbil Gügercinoğlu[1], Meng Guo[16,17], Jason Hessels[18,19], Jiale Hu[17], Guodong Li[1], Mengmeng Ni[17], Jingshan Pan[16,17], Scott M. Ransom[20], Qitong Ruan[17], Ingrid Stairs[21], Chao-Wei Tsai[1], Pei Wang[1], Long Wang[22,23], Na Wang[24], Qingdong Wu[21], Jianping Yuan[24], Jie Zhang[25], Weiwei Zhu[1], Yongkun Zhang[1], and Di Li[1]
[1] National Astronomical Observatories, Chinese Academy of Sciences, A20 Datun Road, Chaoyang District, Beijing 100101, People's Republic of China; leizhang996@nao.cas.cn, dili@nao.cas.cn
[2] Centre for Astrophysics and Supercomputing, Swinburne University of Technology, P.O. Box 218, Hawthorn, VIC 3122, Australia
[3] Max-Planck-Institut für Radioastronomie, Auf dem Hügel 69, D-53121 Bonn, Germany
[4] INAFOsservatorio Astronomico di Cagliari, Via della Scienza 5, I-09047 Selargius (CA), Italy
[5] Guizhou Radio Astronomical Observatory, Guizhou University, Guiyang 550025, People's Republic of China
[6] College of Astronomy and Space Sciences, University of Chinese Academy of Sciences, Chinese Academy of Sciences, Beijing 100101, People's Republic of China
[7] Key Laboratory of Radio Astronomy and Technology, Chinese Academy of Sciences, Beijing 100101, People's Republic of China
[8] Department of Physics, CCIS 4-183, University of Alberta, Edmonton, AB T6G 2E1, Canada
[9] Dipartimento di Fisica e Astronomia "Augusto Righi," Alma Mater Studiorum Università di Bologna, via Piero Gobetti 93/2, I-40129 Bologna, Italy
[10] INAF-Osservatorio di Astrofisica e Scienze dello Spazio di Bologna, Via Piero Gobetti 93/3, I-40129 Bologna, Italy
[11] Yunnan Observatories, Chinese Academy of Sciences, 396 Yangfangwang, Guandu District, Kunming 650216, People's Republic of China
[12] Key Laboratory for the Structure and Evolution of Celestial Objects, Chinese Academy of Sciences, 396 Yangfangwang, Guandu District, Kunming 650216, People's Republic of China
[13] Center for Astronomical Mega-Science, Chinese Academy of Sciences, 20A Datun Road, Chaoyang District, Beijing 100012, People's Republic of China
[14] Purple Mountain Observatory, Chinese Academy of Sciences, Nanjing 210023, People's Republic of China
[15] School of Science, Western Sydney University, Locked Bag 1797, Penrith, NSW 2751, Australia
[16] National Supercomputing Center in Jinan, Qilu University of Technology, 28666 East Jingshi Road, Licheng District, Jinan 250103, People's Republic of China
[17] Jinan Institute of Supercomputing Technology, 28666 East Jingshi Road, Licheng District, Jinan 250103, People's Republic of China
[18] ASTRON, the Netherlands Institute for Radio Astronomy, Oude Hoogeveensedijk 4, 7991 PD Dwingeloo, The Netherlands
[19] Anton Pannekoek Institute for Astronomy, University of Amsterdam, Science Park 904, 1098 XH, Amsterdam, The Netherlands
[20] NRAO, 520 Edgemont Road, Charlottesville, VA 22903, USA
[21] Dept. of Physics and Astronomy, University of British Columbia, 6224 Agricultural Road, Vancouver, BC V6T 1Z1, Canada
[22] School of Physics and Astronomy, Sun Yat-sen University, Daxue Road, Zhuhai, 519082, People's Republic of China
[23] CSST Science Center for the Guangdong-Hong Kong-Macau Greater Bay Area, Zhuhai, 519082, People's Republic of China
[24] Xinjiang Astronomical Observatory, Chinese Academy of Sciences, 150 Science 1-Street, Urumqi, Xinjiang 830011, People's Republic of China
[25] College of Physics and Electronic Engineering, Qilu Normal University, 2 Wenbo Road, Zhangqiu District, Jinan 250200, People's Republic of China
Received 2023 July 26; revised 2023 September 15; accepted 2023 September 15; published 2023 December 4

Abstract

We report on a comprehensive multiwavelength study of the pulsars in the globular cluster (GC) M5, including the discovery of M5G, a new compact noneclipsing "black widow" pulsar. Thanks to the analysis of 34 yr of radio data taken with the Five-hundred-meter Aperture Spherical radio Telescope and Arecibo telescopes, we obtained new phase-connected timing solutions for four pulsars and improved those of the other three. These have resulted in, among other things, (a) much improved proper motions for five pulsars, with transverse velocities (relative to the cluster) that are smaller than their respective escape velocities; (b) 3σ and 1.5σ detections of Shapiro delays in M5F and M5D, respectively; and (c) greatly improved measurement of the periastron advance in M5B, whose value of $\dot{\omega} = 0.^{\circ}01361(6)$ implies that M5B is still likely to be a heavy ($m_p = 1.981^{+0.038}_{-0.088}\ M_{\odot}$) neutron star. The binary pulsars M5D, M5E, and M5F are confirmed to be in low-eccentricity binary systems, the low-mass companions of which are newly identified to be He white dwarfs using Hubble Space Telescope data. Four pulsars are also found to be associated with X-ray sources. Similarly to the eclipsing pulsar M5C, M5G shows little or no nonthermal X-ray emission, indicative of weak synchrotron radiation produced by intrabinary shocks. All seven pulsars known in M5 have short spin periods (<8 ms), and five are in binary systems with low orbital eccentricities. These characteristics differ from the overall GC pulsar population but confirm the expectations for the pulsar population in a cluster with a small rate of stellar encounters per binary system.

Unified Astronomy Thesaurus concepts: Globular star clusters (656); Radio pulsars (1353); Millisecond pulsars (1062)

1. Introduction

Globular clusters (GCs) are among the most prolific targets for radio pulsar searches. Since the discovery of the first GC pulsar (PSR B1821−24A in M28; Lyne et al. 1987), 292 pulsars have been found in 38 different clusters,[26] and these numbers are rapidly growing, especially in the past few years. More than 80% of the GC pulsars are millisecond pulsars (MSPs, defined as $P < 30$ ms), in stark contrast with the 10% MSP fraction of the general Galactic population.[27] Such a contrast can be attributed to the peculiar conditions affecting

[26] https://www3.mpifr-bonn.mpg.de/staff/pfreire/GCpsr.html
[27] http://astro.phys.wvu.edu/GalacticMSPs/GalacticMSPs.txt

stellar evolution in GCs, particularly the large age of the stellar population and the high stellar number densities (10^3–10^7 pc^{-3}) in GC cores, which are many orders of magnitude higher than that in the Galactic field, except for the Galactic center. The resulting high stellar interaction rate favors the dynamical formation of low-mass X-ray binary (LMXB) systems (Clark 1975).

In such interactions, old isolated neutron stars (NSs) in the GC, which had become undetectable after crossing the pulsar "death line" in the P–$\dot{P}$ diagram during their spin-down, can become bound to a low-mass star in a close orbit, and thus become part of an LMXB system. This can happen via tidal capture (Fabian et al. 1975), by exchange encounters (in which the lighter component of a binary system gets replaced by another, most often heavier, star; Hills 1976), or by other mechanisms (Sutantyo 1975). These LMXB formation mechanisms probably happen at a rate that is proportional to the stellar encounter rate Γ of the cluster (Verbunt & Hut 1987).

In an LMXB, the NS can be reactivated by being spun up (or "recycled") to rotation periods of just a few milliseconds through a gigayear-long phase of mass accretion from a light, unevolved donor star, a process that also circularizes the orbit. When accretion stops, we have a fast-spinning radio MSP binary with a low-mass companion in a nearly circular orbit (e.g., Bhattacharya & van den Heuvel 1991), as observed for the population of binary MSPs in the Galactic disk. The evolution of LMXBs in GCs is generally identical. A prime example is 47 Tucanae, where all 29 pulsars currently known are MSPs with periods smaller than 8 ms, and 17 of them are in binary systems with the expected characteristics of the recycling model (e.g., Ridolfi et al. 2016; Freire et al. 2017).

However, in some GCs with a large interaction rate per binary γ, these already-recycled binaries can be disturbed through further strong stellar encounters. This can lead to unbinding of the systems (thus producing a larger fraction of isolated MSPs) or, if the disruption happens during the LMXB stage, to partially recycled pulsars with higher B fields (Verbunt & Freire 2014). In some cases, an exchange encounter may replace the remnant of the star that recycled the pulsar with a heavier degenerate star, which results in a highly eccentric system composed of a pulsar and a heavy companion, such as PSR B2127+11C in M15 (Jacoby et al. 2006), PSR J1835 −3259A in NGC 6652 (DeCesar et al. 2015), and PSR J0514 −4002E in NGC 1851 (Ridolfi et al. 2022). The high-γ GCs containing these exotic binaries are high-density clusters, most of which are designated as core collapsed. Their pulsar populations are remarkably different from GCs like 47 Tuc in their binary parameters.

A GC with a very small γ is M5 (NGC 5904), a bright ($V \approx 5.6$) GC at a distance d of 7.5 kpc (Harris 2010), the nominal center of which is at equatorial coordinates of $\alpha_{J2000} = 15^h18^m\ 33^s.214$, $\delta_{J2000} = +02°\ 04'\ 51''.80$ (Miocchi et al. 2013) in the northern constellation Serpens. The GC core and half-light radii are $\theta_c = 0.44$ and $\theta_h = 1'.77$, respectively. As was visible from the 305 m Arecibo radio telescope in Puerto Rico (USA), it has been extensively observed with that telescope since 1989 at central frequencies of 430 and 1400 MHz. These observations have led to the discovery of five pulsars (Anderson et al. 1997; Mott & Freire 2003; Hessels et al. 2007).

Its decl. makes M5 a promising target for pulsar searches with the Five-hundred-meter Aperture Spherical radio Telescope (FAST; Nan et al. 2011; Li et al. 2018), which can observe over 40 GCs with decl. between −14° and 66° (Zhang et al. 2016). With FAST, Pan et al. (2021) discovered the sixth pulsar in M5 (M5F), which also has a spin period shorter than 8 ms and a circular orbit, as expected for a low-γ cluster.

Except for M5A, the other five (M5B, M5C, M5D, M5E, and M5F) known pulsars in M5 spin very fast and are members of binary systems with low eccentricities and low-mass companions, as might be expected from the low γ of M5. Their dispersion measures (DMs) are between 29.4 and 30.1 pc cm^{-3}, and their 1400 MHz flux densities are estimated to be in the range 0.01–0.12 mJy, although the observed brightness of the pulsars varies significantly owing to diffractive scintillation. Only pulsars A, B, and C have published radio timing phase-connected solutions and optical observations (Anderson et al. 1997; Freire et al. 2008; Pallanca et al. 2014).

In this paper, we present the discovery of a new pulsar (M5G) with FAST. We then present the timing solution of all seven pulsars, combining FAST and Arecibo data, spanning 34 yr. The M5 pulsar population was analyzed with multi-wavelength observations from radio, optical, and X-ray instruments. In Section 2, we describe the observations and data reduction. The discovery, timing solutions, and multi-wavelength emission properties of the pulsars in M5 are presented in Section 3. In Section 4, we discuss the implications of our findings, and we summarize our conclusions in Section 5.

2. Observations

The radio data set is composed of new FAST observations and archival Arecibo data for the GC. A summary of all the radio observations used in this paper is listed in Table 1. We also utilized archival high-resolution near-UV and optical images from the Hubble Space Telescope (HST) and high-energy data from the Chandra X-ray Observatory (CXO). In the following section, we describe the observations made with each telescope.

2.1. FAST Observations

We carried out 33 observations of M5 between 2020 November 16 and 2022 December 14 using the central beam (the beamwidth is 3′ at 1250 MHz) of the FAST 19-beam receiver through three observing projects (PT2020_0074, PT2021_0061, PT2022_0062). For project PT2020_0074, the telescope was pointed at M5B, at $15^h\ 18^m\ 31^s.46$, $+02°\ 05'\ 15''.30$ (Freire et al. 2008). For the other two projects, the telescope was pointed at the nominal cluster center: $15^h\ 18^m\ 33^s.22$, $+02°\ 04'\ 51''.7$ (Goldsbury et al. 2010). All the FAST observations were recorded with 8 bit sampling every 49 μs in pulsar search mode. In all the observations, the observing band from 1000 to 1500 MHz was split into 4096 frequency channels, and due to bandpass roll-off, the effective band is from 1050 to 1450 MHz.

2.2. Arecibo Observations

The GC M5 was first observed by Arecibo with the 430 MHz Carriage House line-feed receiver between 1989 and 1994 (Anderson et al. 1997). From this data set, we were able to retrieve times of arrival (ToAs) only for the pulsars M5A and M5B. Arecibo observations of M5 resumed in 2001, initially

Table 1
Parameters for M5 Pulsars

Pulsar Name	M5A	M5B	M5C	M5D
Observation and data reduction parameters:				
Solar system ephemeris	DE440	DE440	DE440	DE440
Timescale	TDB	TDB	TDB	TDB
Binary model	⋯	DDGR	BTX	ELL1
Reference epoch for α, δ and ν (MJD)	54,000	54,000	54,000	59,500
MJD range of 430 MHz Arecibo	47,635–49,354	47,635–49,394	⋯	⋯
Data span of 430 Arecibo (days)	1720	1760	⋯	⋯
MJD range of *L*-band Arecibo	52,087–54,685	52,087–55,814	52,483–59,831	53,058–55,814
Data span of *L*-band Arecibo (days)	2599	3728	7349	2757
MJD range of *L*-band FAST	59,169–59,927	59,169–59,927	59,169–59,927	59,169–59,927
Data span of *L*-band FAST (days)	759	759	759	759
Number of TOAs at 430 MHz Arecibo	86	81	⋯	⋯
Residual rms at 430 MHz Arecibo (μs)	48.133	112.715	⋯	⋯
Number of TOAs at *L*-band Arecibo	1340	222	1394	97
Residual rms at *L*-band Arecibo (μs)	8.504	71.272	11.224	23.286
Number of TOAs at *L*-band FAST	132	125	309	165
Residual rms at *L*-band FAST (μs)	1.096	22.092	1.664	12.118
Reduced χ^2	1.011	1.023	1.008	1.015
Measured parameters:				
Flux density at 1.25 GHz (mJy)[a]	0.137(8)	0.033(4)	0.044(2)	0.017(1)
Pulse width at 10% of peak, W_{10} (ms)[a]	0.764	3.715	1.303	1.851
Pulse width at 50% of peak, W_{50} (ms)[a]	0.367	1.024	1.077	0.557
R.A., α (J2000)	15:18:33.32293(1)	15:18:31.4629(2)	15:18:32.78978(2)	15:18:30.43512(6)
Decl., δ (J2000)	+02:05:27.4314(4)	+02:05:15.306(7)	+02:04:47.7850(6)	+02:04:59.712(4)
Proper motion in α, μ_α (mas yr^{-1}, J2000)	4.13(1)	4.0(2)	4.25(2)	4.3(2)
Proper motion in δ, μ_δ (mas yr^{-1}, J2000)	−10.03(3)	−10.9(6)	−9.78(5)	−10.2(6)
Spin frequency, ν (s^{-1})	180.063624055099(2)	125.8345875794094(2)	402.588227988547(4)	334.67467287054(2)
Spin frequency derivative, $\dot{\nu}$ (s^{-2})	$-1.33902(3) \times 10^{-15}$	$5.238(3) \times 10^{-17}$	$-4.22684(4) \times 10^{-15}$	$-2.48423(6) \times 10^{-15}$
Second time derivative of spin frequency, $\ddot{\nu}$ (s^{-3})	$-3.6(2) \times 10^{-27}$	⋯	$-1.3(1) \times 10^{-26}$	⋯
Dispersion measure, DM (cm^{-3} pc)[a]	30.0546(5)	29.469(4)	29.3109(3)	29.371(2)
Orbital period, P_b (days)	⋯	6.85845358(4)	0.08682882871(7)	1.2220885130(2)
Projected semimajor axis, χ (lt-s)	⋯	3.048266(3)	0.0573202(1)	1.596065(4)
Epoch of periastron, T_0 (MJD)	⋯	54,004.02035(3)	52,850.0043442(2)	⋯
Epoch of the ascending node, $T_{\rm asc}$ (MJD)	⋯	⋯	⋯	59,189.3836465(2)
$e \sin\omega$, $\varepsilon_1(10^{-5})$	⋯	⋯	⋯	0.25(30)
$e \cos\omega$, $\varepsilon_2(10^{-5})$	⋯	⋯	⋯	−0.14(19)
Orbital eccentricity, e	⋯	0.137839(2)	0.00[d]	⋯
Longitude of periastron, ω (deg)	⋯	359.894(2)	0.00[d]	⋯
Rate of advance of periastron, $\dot{\omega}$ (deg yr^{-1})	⋯	0.01361(6)	⋯	⋯
Time derivative of χ, $\dot{\chi}$ (10^{-14} lt-s s^{-1})	⋯	2.16(3)	⋯	⋯
Time derivative of P_b, $\dot{P}_b$ (10^{-12} s s^{-1})	⋯	−1.7(18)	⋯	⋯
Orbital frequency, f_b(s^{-1})	⋯	⋯	$1.3329759535(7) \times 10^{-4}$	⋯
First orbital frequency derivative, f_b^1(s^{-2})	⋯	⋯	$-6.3(5) \times 10^{-20}$	⋯
Second orbital frequency derivative, f_b^2(s^{-3})	⋯	⋯	$3.6(2) \times 10^{-27}$	⋯
Third orbital frequency derivative, f_b^3(s^{-4})	⋯	⋯	$-7.8(5) \times 10^{-35}$	⋯
Fourth orbital frequency derivative, f_b^4(s^{-5})	⋯	⋯	$9.2(7) \times 10^{-43}$	⋯
Fifth orbital frequency derivative, f_b^5(s^{-6})	⋯	⋯	$-6.2(5) \times 10^{-51}$	⋯
Sixth orbital frequency derivative, f_b^6(s^{-7})	⋯	⋯	$1.8(2) \times 10^{-59}$	⋯
Derived parameters:				
Position perpendicular offset from center (pc)[b]	1.300	1.286	0.274	1.546
Spin period, P (ms)	5.55359254401101(5)	7.94694065627177(2)	2.48392757283615(2)	2.9879763276464(2)
Spin period first time derivative, $\dot{P}$ (10^{-20} s s^{-1})	4.12985(9)	−0.3308(2)	2.60791(3)	2.60791(3)
Mass function, $f(M_\odot)$	⋯	0.000646530	0.0000268213	0.00292300
Minimum companion mass, $M_{c,\rm min}(M_\odot)$[c]	⋯	0.1114	0.03723	0.1907
Median companion mass, $M_{c,\rm med}(M_\odot)$[c]	⋯	0.1297	0.0431	0.2233

Pulsar Name	M5E	M5F	M5G
Observation and data reduction parameters:			
Solar system ephemeris	DE440	DE440	DE440
Timescale	TDB	TDB	TDB
Binary model	ELL1	ELL1	ELL1
Reference epoch for α, δ and ν (MJD)	59,500	59,500	59,500

Table 1
(Continued)

Pulsar Name	M5E	M5F	M5G
MJD range of 430 MHz Arecibo	…	…	…
Data span of 430 Arecibo (days)	…	…	…
MJD range of *L*-band Arecibo	53,029–54,685	…	…
Data span of *L*-band Arecibo (days)	1656	…	…
MJD range of *L*-band FAST	59,169–59,927	59,169–59,927	59,169–59,927
Data span of *L*-band FAST (days)	759	759	759
Number of TOAs at 430 MHz Arecibo	…	…	…
Residual rms at 430 MHz Arecibo (μs)	…	…	…
Number of TOAs at *L*-band Arecibo	104	…	…
Residual rms at *L*-band Arecibo (μs)	10.141	…	…
Number of TOAs at *L*-band FAST	188	110	161
Residual rms at *L*-band FAST (μs)	3.431	6.337	6.747
Reduced χ^2	1.003	1.004	1.013
Measured parameters:			
Flux density at 1.25 GHz (mJy)[a]	0.022(3)	0.012(3)	0.008(1)
Pulse width at 10% of peak, W_{10} (ms)[a]	2.288	2.102	0.555
Pulse width at 50% of peak, W_{50} (ms)[a]	0.875	1.711	0.133
R.A., α (J2000)	15:18:33.3027(4)	15:18:32.3948(3)	15:18:28.72895(9)
Decl., δ (J2000)	+02:04:37.954(2)	+02:05:12.07(1)	+02:05:15.040(4)
Proper motion in α, μ_α (mas yr^{-1}, J2000)	4.04(12)	…	…
Proper motion in δ, μ_δ (mas yr^{-1}, J2000)	−10.35(26)	…	…
Spin frequency, ν (s^{-1})	314.23809500370(1)	376.7625236987(2)	363.61166596073(2)
Spin frequency derivative, $\dot{\nu}$ (s^{-2})	$-1.77140(4) \times 10^{-15}$	$-3.14(2) \times 10^{-15}$	$-1.649(3) \times 10^{-15}$
Second time derivative of spin frequency, $\ddot{\nu}$ (s^{-3})	…	$5.2(15) \times 10^{-24}$	…
Dispersion measure, DM (cm^{-3} pc)[a]	29.310(1)	29.409(1)	29.3945(7)
Orbital period, P_b (days)	1.09693224035(8)	1.609518449(2)	0.1139283090(6)
Projected semimajor axis, χ (lt-s)	1.1516157(8)	1.953013(2)	0.0359535(8)
Epoch of the ascending node, $T_{\rm asc}$ (MJD)	59,198.0057398(1)	59,202.4806455(5)	59,204.7170718(9)
$e \sin\omega$, $\varepsilon_1(10^{-5})$	−0.78(15)	−0.31(17)	0.00[d]
$e \cos\omega$, $\varepsilon_2(10^{-5})$	0.14(12)	−0.25(16)	0.00[d]
Derived parameters:			
Position perpendicular offset from center (pc)[b]	0.502	0.867	2.591
Spin period, P (ms)	3.1823003509114(1)	2.654191797482(1)	2.7501867888583(1)
Spin period first time derivative, $\dot{P}$ (10^{-20} s s^{-1})	1.79390(4)	2.21(1)	1.247(2)
Mass function, $f(M_\odot)$	0.001362843	0.00308749	0.0000038445
Minimum companion mass, $M_{c,\rm min}$ ($M_\odot$)[c]	0.145	0.1946	0.01932
Median companion mass, $M_{c,\rm med}$ ($M_\odot$)[c]	0.1692	0.2279	0.0223

Notes. Numbers in parentheses represent uncertainties on the last digit.
[a] Parameter derived from FAST data only.
[b] The pulsar's position is offset from the nominal cluster center ($15^{\rm h}\,18^{\rm m}\,33^{\rm s}.22$, $+02^\circ\,04'\,51''.7$) for a cluster distance 7.5 kpc.
[c] The companion masses are derived from radio timing and assume a pulsar mass of 1.4 $M_\odot$. The minimum and median masses assume an inclination angle of 90° and 60°, respectively.
[d] Because of the small semimajor axis and the presence of eclipses or dispersive delays, eccentricity measurements in black widow systems have large uncertainties and are unreliable. In these systems, it is expected that tidal dissipation keeps orbits circular. In this work, we have assumed that this is indeed the case.

using the "old" Gregorian *L*-band receiver (2001–2003) and later using the "new" and more sensitive Gregorian *L*-band receiver (2003–2008). For details on the exact observing setup and recording modes, we refer to Freire et al. (2008). From the other two data sets, we were able to retrieve most of the observations, archived as PRESTO[28] sub-banded files, i.e., search-mode files that were greatly reduced in size by summing groups of frequency channels after dedispersing at the DMs of pulsars A–E.

2.3. Hubble Space Telescope

We analyzed deep and high-resolution near-UV and optical observations obtained with the Advanced Camera for Surveys and the Wide Field Camera 3 on board HST through six different filters: F275W, F336W, F390W, F435W, F606W, and F814W. These observations were carried out as part of different HST proposals: GO-12517 (PI: Ferraro), GO-11615 (PI: Ferraro), GO-15875 (PI: Bellini), GO-10615 (PI: Anderson), and GO-13297 (PI: Piotto).

The data reduction was performed using DAOPHOT IV (Stetson 1987, 1994) on the calibrated images and adopting the so-called "UV-route." Details on the data reduction routines can be found in Chen et al. (2021; see also Cadelano et al. 2020a, 2020b; Chen et al. 2023). The instrumental magnitudes were calibrated to the VEGAMAG photometric system by using appropriate zero-points and aperture corrections. We transformed the instrumental positions of the sources to the International Celestial Reference System by cross-correlating our catalog with the Gaia Data Release 3 catalog of stars (Gaia

[28] https://github.com/scottransom/presto

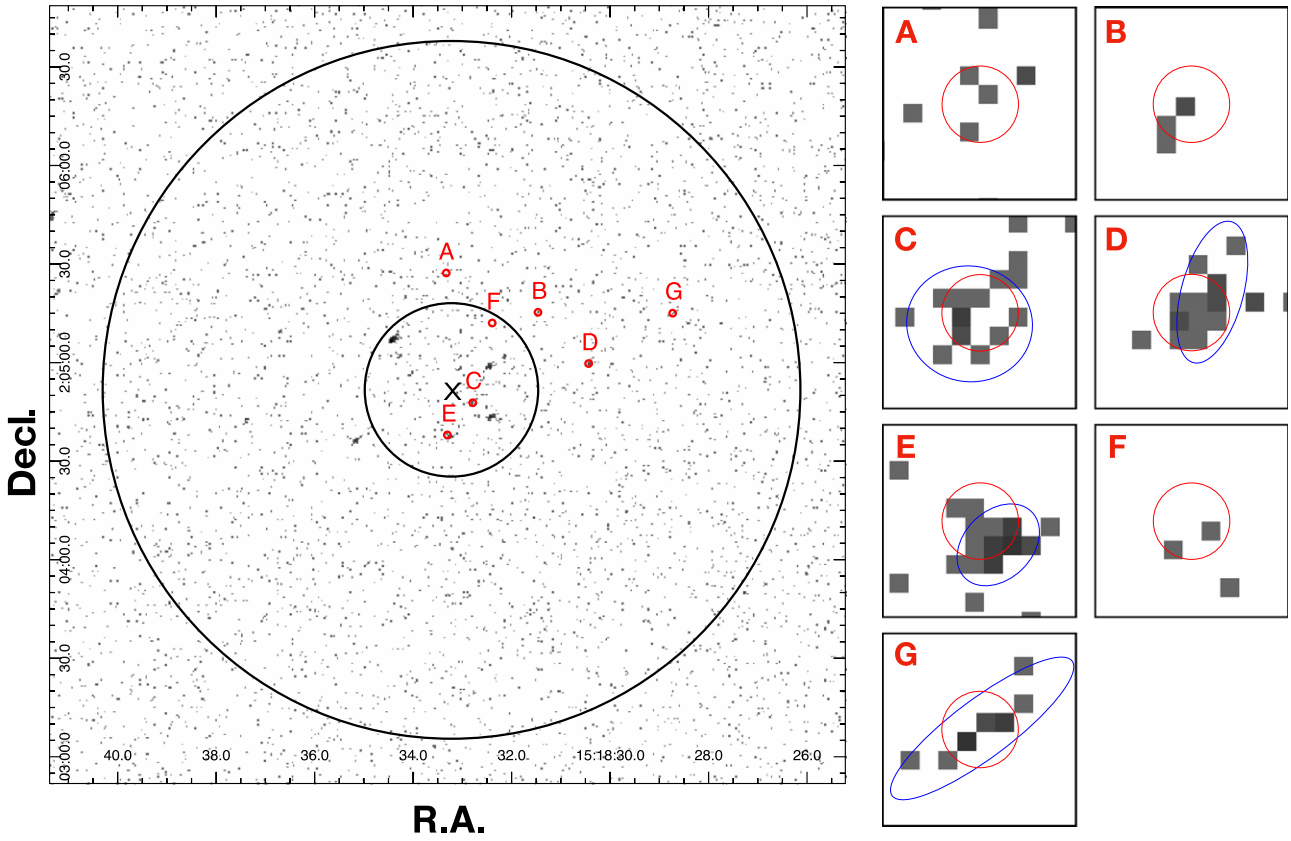

Figure 1. Left: Chandra X-ray image of M5 in the 0.3–8 keV energy band. The two concentric black circles with radii of 0.′ 44 and 1.′ 77 show the core radius and half-light radius, respectively, centered at R.A. = 15:18:33.22, decl. = +02:04:51.7 (black cross; Goldsbury et al. 2010). The MSP locations are labeled with 1″-radius red circles centered at their corresponding timing positions, with pulsar names annotated above. Right: zoom-in images of M5 MSPs in 5″ × 5″ boxes. Blue ellipses show the source detections by `wavdetect` (Table 5). X-ray counterparts are found to MSPs C, D, E, and G, whereas no X-ray sources are detected around MSPs A, B, and F.

Collaboration et al. 2023). The residuals of this transformation returned a combined rms of ∼15 mas, which was adopted as the 1σ astrometric accuracy.

2.4. Chandra X-Ray Observatory

M5 has been observed by CXO with an exposure time of 44.7 ks in the FAINT data mode (Observation ID 2676). Figure 1 (left panel) shows the X-ray image of M5 in the band 0.3–8 keV. The X-ray counterpart to M5C was identified by Zhao & Heinke (2022), whereas no X-ray counterparts were found for M5A and M5B. Here, using our new timing positions of M5 MSPs, particularly the four MSPs with newly derived timing solutions, we searched for their X-ray counterparts using the Chandra observation.

3. Analyses and Results

3.1. Discovery of M5G and Timing Analysis

We searched for new MSPs in the FAST observations using the PRESTO software suite (Ransom et al. 2002), with a Fourier-domain jerk search with a maximum linear Fourier drift rate $z_{\rm max} = 200$ and a maximum Fourier jerk drift rate $w_{\rm max} = 300$ (see Andersen & Ransom 2018). We also split the long observations (more than 2 hr) into 15, 30, and 60 minute blocks so as to be sensitive to orbits with orbital periods as short as ∼2 hr (Ng et al. 2015). We found a 2.7 ms pulsar signal at a DM of 29.4 pc cm^{-3} in multiple observations, each time with a different associated acceleration, suggesting the presence of a binary motion. Being the seventh pulsar known in the cluster, the pulsar was named M5G (or PSR J1518+0204G). Of the 33 follow-up observations, M5G was detected on 30 occasions, over the span of 2 yr. The nondetections are most likely attributable to unfavorable scintillation.

In order to characterize M5G, we performed a radio timing analysis as follows. First, we folded each search-mode observation with 60 s subintegrations and 128 profile bins using DSPSR[29] (van Straten & Bailes 2011). We removed data affected by radio frequency interference in both the frequency and time domains. After that, for each folded archive, we summed groups of frequency channels and subintegrations so as to have sufficiently high signal-to-noise ratio integrated profiles, which were then cross-correlated with a profile template to extract pulse ToAs using the *pat* routine from the PSRCHIVE[30] (Hotan et al. 2004) package. The TEMPO2 (Hobbs et al. 2006) timing software was then used to develop a comprehensive timing model of the pulsar's behavior, including its position, rotation, and a binary model ELL1 (Lange et al. 2001) that assumes low orbital eccentricity. These procedures were iterated a few times until a phase-connected timing solution was obtained. The DM was measured with TEMPO2 using ToAs from multifrequency subbands. The timing solution of pulsar M5G is presented in Table 1. In Figure 2, the timing residuals are shown as

[29] http://dspsr.sourceforge.net
[30] http://psrchive.sourceforge.net

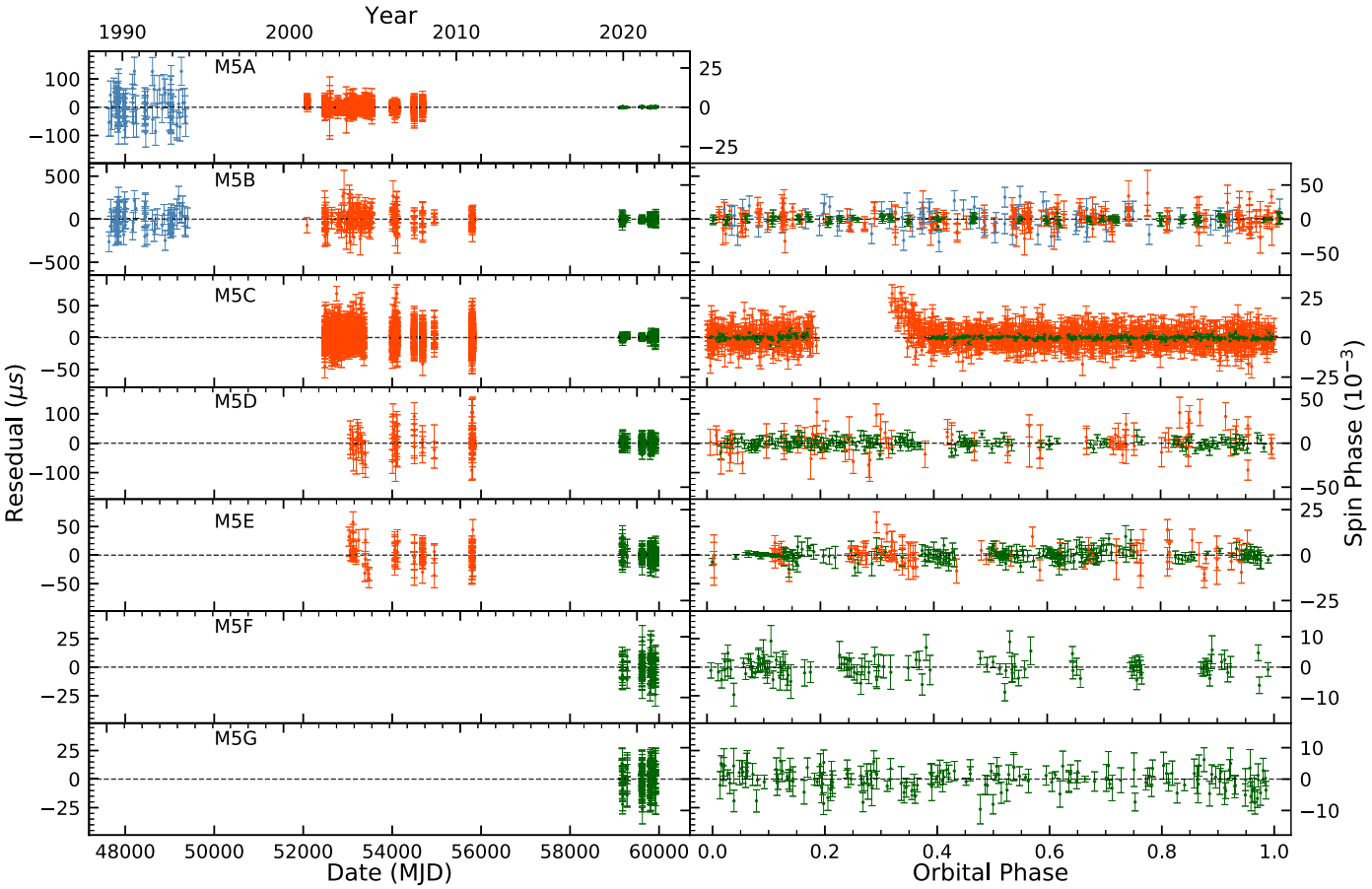

Figure 2. Timing residuals of the seven MSPs in M5 obtained using the timing solutions in Table 1. The left panels show the post-fit timing residuals as a function of time, whereas the right panels show the post-fit timing residuals as a function of orbital phase for the binary pulsars (i.e., all except M5A). The blue, orange, and green points represent observations taken with Arecibo at 430 MHz, Arecibo at *L* band, and FAST at *L* band, respectively.

functions of time and orbital phase: as can be seen, its radio pulsations can be detected at all orbital phases. M5G is a noneclipsing "black widow"–type binary MSP, with an orbital period of 2.73 hr and a companion mass of around 0.02 $M_\odot$, if we assume that the pulsar has a mass of ∼1.4 $M_\odot$.

3.2. Timing of Known MSPs

Six pulsars had been discovered in previous observations of M5. The timing solutions of M5A, M5B, and M5C were published by Freire et al. (2008) and Pallanca et al. (2014), but have not been updated since. There are no published timing solutions for M5D, M5E, and M5F, even though pulsars D and E were discovered in 2007. To time those pulsars, we first attempted to fold our data using the ephemerides from the ATNF pulsar catalog.[31] However, we found that those ephemerides are not accurate enough to keep phase coherence in our data, except for M5A. Thus, to detect M5B to M5F for each epoch of observation, we performed a blind search for their periodic signal and then folded the data using the local ephemerides derived from the search. Once the detections were made, we then followed the procedures as described in Section 3.1 to obtain an accurate timing solution for all six pulsars. The timing solutions and residuals of these pulsars are summarized in Table 1 and shown in Figure 2, respectively. The timing parameters are reported in dynamical barycentric time (TDB), and we have used the Jet Propulsion Laboratory's DE440 solar system ephemeris (Park et al. 2021) for all pulsars.

3.3. Pulse Profiles and Flux Densities

To probe the pulsed emission properties of all seven pulsars, we again used programs from the PSRCHIVE package. We constructed average pulse profiles by summing the FAST observations in time using the timing solution of the pulsar to ensure phase alignment. We present the average profiles at 1.25 GHz in Figure 3. The pulse widths at 50% (W_{50}) and 10% (W_{10}) of the pulse peak were measured using the program PDV from noise-free profiles obtained using the program PAAS, while we estimated each pulsar's flux density at 1.25 GHz using the radiometer equation. The W_{50}, W_{10}, and flux density estimates for the M5 pulsars are also listed in Table 1.

3.4. Update on Mass Measurement for M5B

One of the main results published by Freire et al. (2008) was the measurement of the rate of periastron advance for M5B, $\dot{\omega} = 0.^\circ 0142(7)\ \mathrm{yr}^{-1}$, which was made possible by its relatively large orbital eccentricity, $e = 0.138$, by far the largest among the known binary pulsars in the cluster. Assuming that this effect is purely relativistic (an assumption based on the nondetection of the companion to the pulsar in HST images; see also Section 3.8) and that general relativity (GR) is the correct theory of gravity, this translated into a total mass $M_T = 2.29 \pm 0.17\ M_\odot$. Given the low mass function of

[31] https://www.atnf.csiro.au/research/pulsar/psrcat/

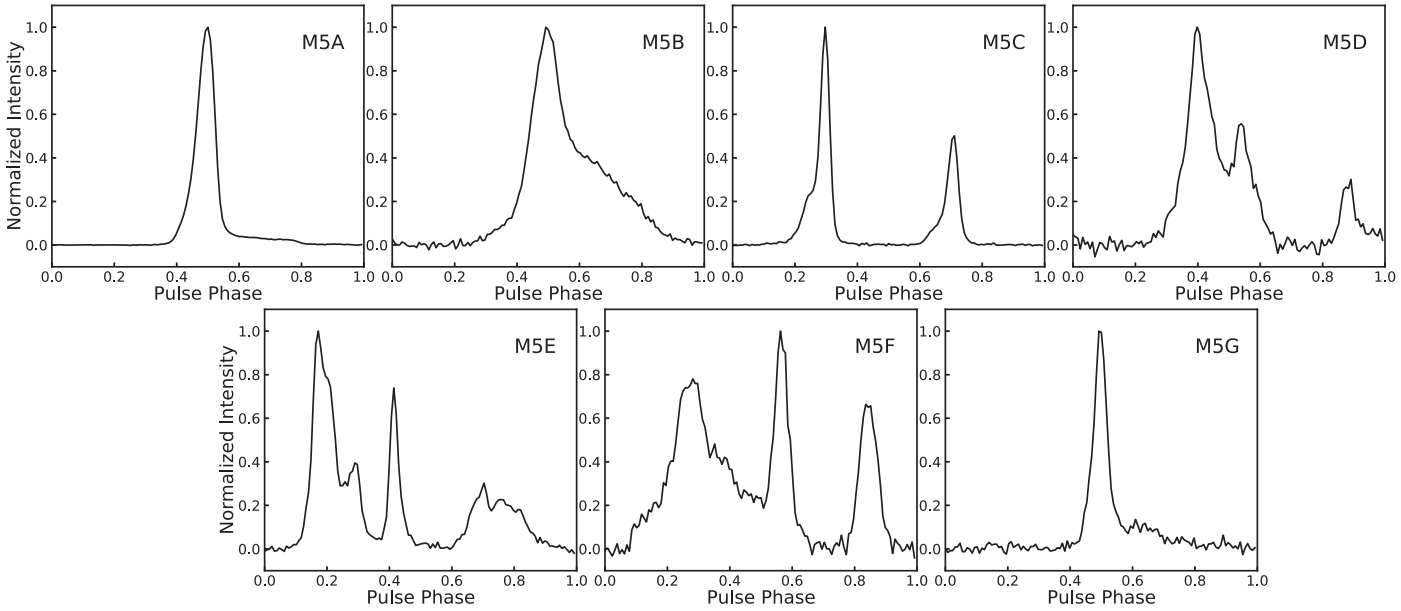

Figure 3. Integrated profiles of the seven pulsars in M5 from FAST data at 1.25 GHz.

the system, a statistical analysis that assumes a priori randomly aligned orbits implied a large mass for the pulsar, $M_T = 2.08 \pm 0.19\,M_\odot$, with a 95% probability of a mass above $1.72\,M_\odot$ and only a 0.77% probability of a mass within the range of pulsar masses then known, 1.2–1.44 $M_\odot$. This was an early indication that NSs could have masses substantially above $1.44\,M_\odot$. However, apart from their unlikelihood, there is no physical measurement that precludes the occurrence of a lower orbital inclination. In addition, in a large set of binary systems in GCs, some should be seen with a range of low orbital inclinations.

The inclusion of additional observations has greatly improved the astrometric, spin, and orbital parameters of M5B. However, apart from an order-of-magnitude improvement of the rate of periastron advance ($\dot{\omega} = 0.^\circ 01361(6)\ \mathrm{yr}^{-1}$, which is 1σ compatible with the value presented by Freire et al. 2008), no additional relativistic effects have been detected. Such effects, like the Einstein delay (γ_E) or the Shapiro delay (Shapiro 1964), are required for determinations of the individual component masses.

In order to try to detect additional post-Keplerian parameters to allow estimates of the masses, we have made a χ^2 map of the m_c–cos i space, following the Bayesian procedure described in detail by Splaver et al. (2002). To sample the space, we used the DDGR timing solution (Damour & Deruelle 1986), which self-consistently accounts for all relativistic effects in the timing, even if they are present at a very low level, with the assumption that GR is the correct gravity theory. Given the precise constraint on $\dot{\omega}$, we restrict the m_c–cos i space being sampled to values of the total mass that are not too different from the new GR estimate of the total mass derived from $\dot{\omega}$.

The results for the 2D posterior probability density functions (pdfs) in the m_c–cos i and m_c–m_p planes are depicted in the main panels of Figure 4, where the contours include, respectively, 63.28%, 95.45%, and 99.72% of probability. From these posterior 2D pdfs, we derive 1D posterior pdfs for a few quantities. From their medians and $\pm1\sigma$ equivalent percentiles, we derive $m_c = 0.163^{+0.095}_{-0.020}\,M_\odot$, $m_p = 1.981^{+0.038}_{-0.088}\,M_\odot$, and $M_T = 2.157^{+0.028}_{-0.027}\,M_\odot$. From the 2σ equivalent percentiles, we derive $m_c = 0.163^{+0.457}_{-0.023}\,M_\odot$, $m_p = 1.981^{+0.070}_{-0.409}\,M_\odot$, and $M_T = 2.157 \pm 0.055\,M_\odot$. Again, these values are consistent with those derived by Freire et al. (2008). The pulsar could still have a mass similar to the largest NS masses that have been reliably determined (PSR J0348+0432, $m_p = 2.01 \pm 0.04\,M_\odot$, Antoniadis et al. 2013; and PSR J0740+6620, $m_p = 1.99 \pm 0.07\,M_\odot$, Fonseca et al. 2021), but not larger.

As we can see in the top left panel of Figure 4, there is no constraint on the orbital inclination, with the median of the cos i pdf appearing very close to 0.5. This indicates that, apart from the obvious fact that the Shapiro delay is not detectable (thus excluding orbital inclinations close to 90°), there are no additional detectable relativistic effects in the timing data. This means that, apart from the small likelihood of lower inclinations (which stems from their small range of cos i), no measured relativistic effect precludes a substantially smaller pulsar mass and larger companion mass.

Given the fact that we are already timing M5 with FAST and that 34 yr have elapsed since discovery, the prospects for the determination of additional post-Keplerian parameters and individual mass measurements for this system appear poor in the foreseeable future. Given the low orbital eccentricities of the remaining binaries, the prospect of $\dot{\omega}$ measurements for them is even more distant.

3.5. Detection of the Shapiro Delay of M5F and Possibly of M5D

If we use the orthometric parameterization of the Shapiro delay (Freire & Wex 2010) to fit for the Shapiro delay in M5F, we obtain a stable convergence at $\varsigma = 0.982 \pm 0.043$ and $h_3 = 0.95 \pm 0.43\,\mu$s for the orthometric ratio and amplitude, respectively. If we fix ς at this value, we obtain $h_3 = 0.95 \pm 0.34\,\mu$s, indicating a nearly 3σ detection of the Shapiro delay. This detection points to a very high inclination (close to 89°), $m_c \sim 0.2\,M_\odot$, and $m_p \sim 1.4\,M_\odot$, but still with large (∼50%) relative uncertainties in m_c. These values are consistent with the optical values derived below in Section 3.8, seen in particular in the right panel of Figure 9. They are also consistent, within their wide uncertainties, with the $0.22\,M_\odot$ predicted by Tauris &

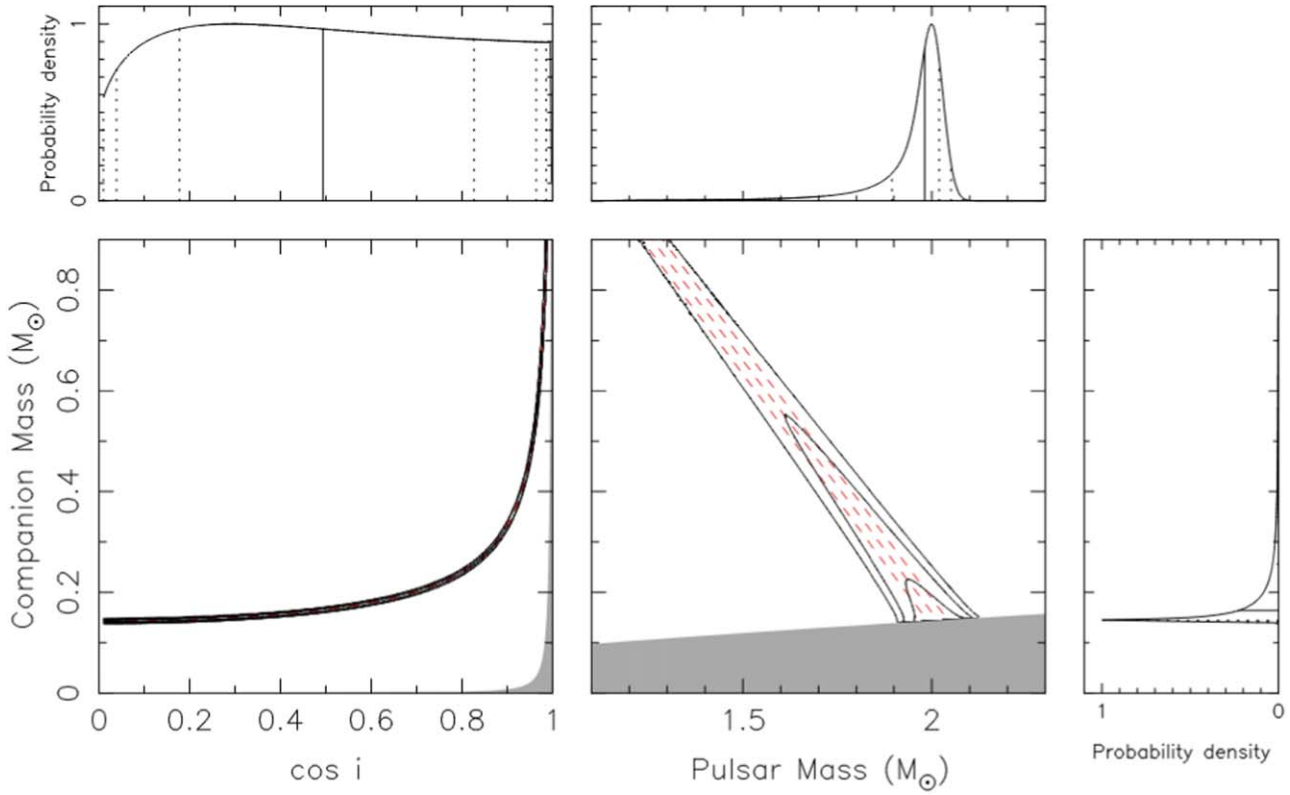

Figure 4. Mass constraints for the M5B binary system. In the main panels, we show the m_c–cos i and m_c–m_p planes. In the left panel, the gray zone is excluded because m_p must be >0; in the right panel, the gray zone is excluded because sin i must be ⩽1. The contours include, respectively, 63.28%, 95.45%, and 99.72% of all probability in the 2D posterior pdfs. The red dashed lines represent the median and $\pm 1\sigma$ constraints on the total mass derived from the measurement of the rate of advance of periastron ($\dot{\omega}$). In the side panels, the curves show the 1D pdfs for cos i, m_p, and (in the right panel) m_c; these medians are indicated by the solid lines; the equivalent 1σ, 2σ, and 3σ percentiles are indicated by the dashed lines.

Savonije (1999) for a helium white dwarf (WD) derived from Population II stars in a binary with the orbital period of M5F. A 1.5σ h_3 is also seen in the timing of M5D. An intense, well-coordinated FAST campaign might possibly measure the masses in the M5F system (and possibly in M5D) via Shapiro delay.

3.6. Proper Motions

Because of the increased timing baselines, the proper motions for M5A, M5B, and M5C are significantly more precise than previous published values for these pulsars. With a timing baseline of ∼19 yr for M5D and M5E, we have also measured their proper motions. The smaller timing baselines for M5F and M5G, which are only detectable in FAST data, preclude a significant detection of the proper motion. The (unweighted) average proper motion for the first five pulsars in R.A. and decl. is $\mu_\alpha = 4.14\,\mathrm{mas\,yr^{-1}}$ and $\mu_\delta = -10.25\,\mathrm{mas\,yr^{-1}}$, respectively. The standard deviations of the proper motions around this mean (σ_μ) are 0.3 mas yr^{-1} in μ_α and 0.89 mas yr^{-1} in μ_δ. The uncertainty in the mean value is given by $\sigma_\mu/\sqrt{N}$, where N is the number of measurements (5 in this case). Thus, our uncertainties for the mean cluster motion are $\sigma_{\mu,\alpha} = 0.14\,\mathrm{mas\,yr^{-1}}$ and $\sigma_{\mu,\delta} = 0.4\,\mathrm{mas\,yr^{-1}}$. At the distance to M5, these rms values translate to velocity dispersions of ∼5 and ∼14 km s^{-1}, which are of a similar order of magnitude to the stellar velocity dispersion ($\sigma_S = 7.7\,\mathrm{km\,s^{-1}}$; Baumgardt & Hilker 2018; Kamann et al. 2018; Lanzoni et al. 2018). However, the larger rms in decl. is also likely to be caused, in part, by the larger uncertainties of the proper motions along that direction.

The proper motions of these five pulsars are depicted in Figure 5, and the mean cluster motion along with the uncertainty is marked by the Earth symbol. According to the latest study based on the Gaia EDR3 data, Vasiliev & Baumgardt (2021) derived M5's absolute proper motion as $\mu_\alpha = 4.086 \pm 0.023\,\mathrm{mas\,yr^{-1}}$ and $\mu_\delta = -9.870 \pm 0.023\,\mathrm{mas\,yr^{-1}}$. This is consistent with our measurement of the average proper motion, if we take the latter's uncertainty into account. As we can see in Figure 5, all measured proper motions fall within the circle defined by the optical proper motion and the central escape velocity of M5, 29.9 km s^{-1} (Baumgardt & Hilker 2018), with the exception of M5B. However, the latter still has a large uncertainty in its proper motion; its error ellipse overlaps with regions well within the escape velocity from the cluster. The best-measured proper motions (those of M5A and M5C) are the ones closer to the Gaia EDR3 proper motion.

3.7. Acceleration in the Cluster Field

In Table 1, we see that one of the pulsars (M5B) has a negative $\dot{P}$. Radio MSPs are rotationally powered, so their intrinsic spin period derivative $\dot{P}_{\rm int}$ should be positive. The observed spin period derivative is given by Phinney (1993):

$$\left(\frac{\dot{P}}{P}\right)_{\rm obs} = \left(\frac{\dot{P}}{P}\right)_{\rm int} + \frac{\mu^2 d}{c} + \frac{a_{l,\rm GC}}{c} + \frac{a}{c}, \qquad (1)$$

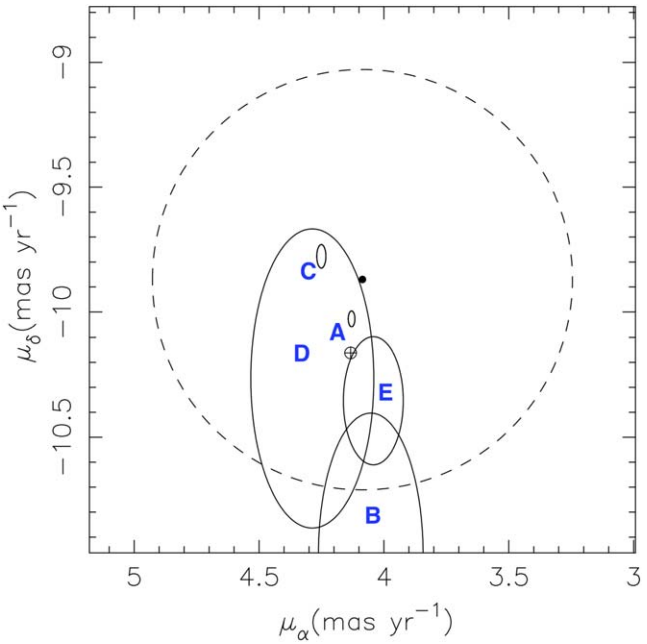

Figure 5. Proper motions of the pulsars in M5. The error ellipses depict the 1σ uncertainties for their proper motion in α and δ. The central filled circle is the proper motion derived from Gaia EDR3 measurements; the dashed circle around it depicts the escape velocity from the cluster. The Earth symbol ($\oplus$) depicts the average of the pulsar proper motions.

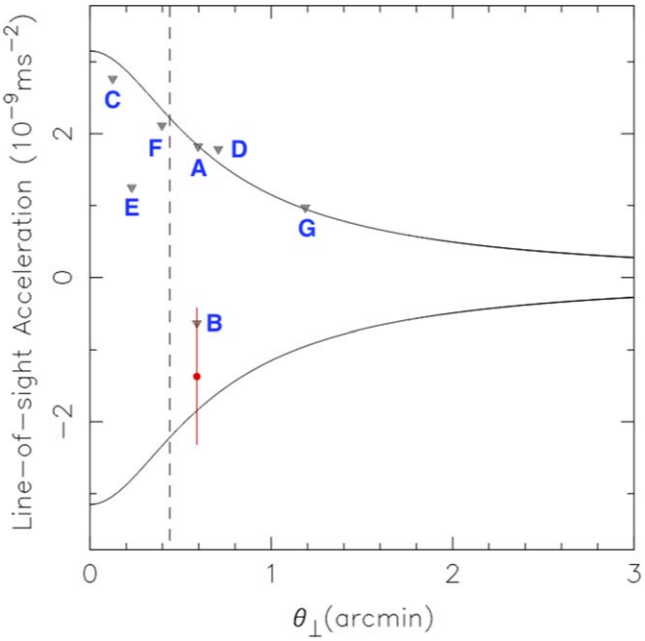

Figure 6. Upper limits for the line-of-sight accelerations of the M5 pulsars (triangles) as a function of their angular distance from the nominal cluster center ($\theta_\perp$), derived from $\dot{P}_{\rm obs}$. The solid black curves indicate the maximum and minimum accelerations along the line of sight caused by the potential of the GC predicted by the analytical model described in the text. The red filled circle and its error bar indicate the acceleration (and its uncertainty) derived from the orbital period derivative of M5B. The vertical dashed line indicates the core radius.

where μ is the total proper motion of the system (for pulsars where this is not used, we used the proper motion of M5 discussed above), d is the distance to the cluster ($\mu^2 d/c$ is the so-called Shklovskii effect; Shklovskii 1970), c is the speed of light, $a_{l,\rm GC}$ is the line-of-sight acceleration of the pulsar in the gravitational field of the cluster, and a is the line-of-sight difference of the Galactic acceleration of the center of mass of M5 and that of the solar system barycenter. Using the McMillan (2017) mass model of the Galaxy, we obtain, for the position of M5, $a = -0.233 \times 10^{-9}\,{\rm m\,s^{-2}}$.

The acceleration caused by the gravitational potential of the GC, $a_{l,\rm GC}$, is generally the dominant contribution. To model this, we used an analytical model of the cluster described in Freire et al. (2005), which is based on the empirical King (1962) density profile. The line-of-sight acceleration due to the cluster potential at distance x from the center (in core radii) and distance l from the plane of the sky passing through the center of the GC (also in core radii) is given by

$$a_{l,\rm GC}(x) = \frac{9\sigma_{\rm S}^2}{d\theta_c}\frac{l}{x^3}\left(\frac{x}{\sqrt{1+x^2}} - \sinh^{-1}x\right). \quad (2)$$

The parameters for this model include the position, distance, and core radius of M5 (see Section 1) and the aforementioned central stellar velocity dispersion. In Figure 6, the solid black curves represent the maximum and minimum values of $a_{l,\rm GC}(x)$ for each angular offset from the center, $\theta_\perp$.

For each pulsar, if we assume a negligible intrinsic spin-down, we can derive an absolute upper limit for its acceleration in the field of the GC:

$$a_{l,\rm P,max} = c\frac{\dot{P}_{\rm obs}}{P} - \mu^2 d - a, \quad (3)$$

where, if the pulsar does not have a well-measured proper motion, we used the proper motion for the cluster measured by Vasiliev & Baumgardt (2021). The upper limits appear in Figure 6 as the triangles; the values of these accelerations are also listed in Table 2.

From this figure, we conclude that, despite the small accelerations predicted by the analytical model described above, it can account for the negative $\dot{P}_{\rm obs}$ of M5B (for the line-of-sight acceleration to be negative, this binary must be located in the more distant half of the cluster). The model cannot fully account for the positive $a_{l,P,\rm max}$ of pulsars M5D and M5G, but this is to be expected because their $\dot{P}_{\rm obs}$ has a contribution from a positive $\dot{P}_{\rm int}$.

Taking the maximum and minimum theoretical accelerations caused by the gravitational field of the GC for the line of sight of each pulsar, we can calculate maximum (and in some cases minimum) limits for the $\dot{P}_{\rm int}$ of each pulsar; from these we can derive extreme limits for their magnetic fields and characteristic ages. These values are also presented in Table 2.

An estimate of the intrinsic spin-down can also be derived from the observed orbital period derivative of M5B. Given its P_b of 6.85 days, low eccentricity, and small companion mass, the intrinsic variation caused by GW emission is negligible, so any variations of P_b are caused by the last three terms in an equation similar to Equation (1). Subtracting the latter equation from Equation (1), we obtain

$$\left(\frac{\dot{P}}{P}\right)_{\rm int} = \left(\frac{\dot{P}}{P}\right)_{\rm obs} - \left(\frac{\dot{P}_b}{P_b}\right)_{\rm obs}, \quad (4)$$

Table 2
Derived Parameters for M5 Pulsars

Pulsar Name	$a_{l,\mathrm{P,max}}$ (10^{-9} m s^{-2})	$a_{l,\mathrm{GC,max}}$ (10^{-9} m s^{-2})	$\dot{P}_{\mathrm{int}}$ (10^{-20} s s^{-1})	B (10^{9} G)	τ_c (Gyr)
A	+1.82	1.83	0–6.76	0–0.62	1.3–∞
B	−0.64	1.84	0–3.20	0–0.51	3.9–∞
C	+2.76	3.03	0–4.80	0–0.35	0.8–∞
D	+1.78	1.60	0.19–3.37	0.08–0.32	1.4–25
E	+1.25	2.80	0–4.30	0–0.37	1.2–∞
F	+2.11	2.34	0–3.93	0–0.33	1.1–∞
G	+0.97	0.95	0.02–1.76	0.02–0.22	2.5–247

Note. For each of the pulsars in M5, we calculate an upper limit for the pulsar accelerations in the field of the GC, theoretical upper and lower limits for the line-of-sight acceleration due to the cluster potential, the resulting limits on the intrinsic spin period derivative, and extreme limits for the surface magnetic field strength (B) and the characteristic age (τ_c), respectively (see text for details).

from which we obtain $\dot{P}_{\mathrm{int}} = (1.9 \pm 2.5) \times 10^{-20}$. From the nominal value we obtain $B_0 \sim 4 \times 10^8$ G and $\tau_c \sim 6.5$ Gyr; however, given the large relative uncertainty in $\dot{P}_{\mathrm{int}}$, these values are still very crude approximations.

The fact that the majority of pulsars have positive $\dot{P}_{\mathrm{obs}}$ suggests that the positive $\dot{P}_{\mathrm{int}}$ are of a similar magnitude to the effect of the GC acceleration; otherwise, about half of pulsars would have negative $\dot{P}_{\mathrm{obs}}$, as observed for GCs with much larger predicted accelerations, like 47 Tuc (Freire et al. 2017; Abbate et al. 2018) or Terzan 5 (Prager et al. 2017). However, this is still small number statistics: even if all $\dot{P}_{\mathrm{int}}$ were very small compared to the accelerations, there would still be a 5% probability (using Gehrels 1986, Table 6) that only one out of seven has a negative acceleration.

The main conclusion to be taken from this analysis is that, even though the individual accelerations in the gravitational field of M5 are not known for most pulsars, the predicted accelerations have a rather small range. From this and the measured $\dot{P}_{\mathrm{obs}}$, we conclude that $B_0 < 6.2 \times 10^8$ G and $\tau_c > 0.8$ Gyr. This is consistent with the characteristics of the MSP population in the Galactic disk.

3.8. Optical Counterparts to MSPs

In previous works, two of the binary MSPs in M5 have been studied at optical wavelengths. The companion of M5B is not detectable (Freire et al. 2008), a result that was important to establish that the observed periastron advance is relativistic, which we confirm below. However, the low-mass companion of the M5C "black widow" system has been detected (Pallanca et al. 2014), showing the photometric variability with orbital phase that is characteristic of such systems.

In order to identify the undetected optical counterparts to the remaining binary MSPs, we investigated all stars located around their positions. At the corresponding positions of M5D, M5E, and M5F we found three blue objects that in the color–magnitude diagrams (CMDs) are located along the red side of the WD cooling sequence in all the available filter combinations (see an example in Figure 8). This is the CMD position where He-core WDs (He WDs), i.e., the typical outcome of the evolution of binary MSPs, are located. All the companions are located at distances between 50 and 60 mas from the corresponding pulsar positions. Such distances are larger than the combined optical and radio position uncertainties. However, the three candidate counterparts are systematically shifted toward the northwest direction, suggesting an offset between the radio and optical frames. The average shift along R.A. and decl. is $-0\farcs03$ and $0\farcs05$, respectively. After accounting for such a shift, all three WDs are located at distances between 4 and 15 mas from the pulsar positions. We detected no stars at the corresponding positions of M5B and M5G. The finding charts of the five investigated objects, after accounting for the radio−optical offset, are presented in Figure 7. Magnitudes and upper limits are listed in Table 3.

To confirm the He WD nature of the three counterparts and derive their physical properties, we compared their magnitudes obtained in different filters with those predicted by binary evolution models. First, we performed a photometric calibration sanity check in all the available filter combinations by comparing the standard evolutionary sequences with a 12.5 Gyr isochrone extracted from the BaSTI database (Hidalgo et al. 2018; Pietrinferni et al. 2021) assuming [Fe/H] = −1.3 (Harris 1996, 2010 edition). We also compared the position of the observed WD cooling sequence with a theoretical cooling track extracted from the BaSTI database (Salaris et al. 2022) for CO WDs with a typical mass of 0.55 $M_\odot$. Absolute magnitudes were converted to the observed frame assuming a distance modulus $(m - M)_0 = 14.37$ and a color excess $E(B - V) = 0.03$ (Harris 1996, 2010 edition) and using appropriate extinction coefficients from Cardelli et al. (1989) and O'Donnell (1994). All the evolutionary sequences are well reproduced by the adopted models in all the filter combinations (see the black curves in Figure 8).

In order to constrain the properties of the companion stars, we exploit the binary evolution models from the database described in Istrate et al. (2014, 2016). Theoretical luminosities and temperatures were converted to observed magnitudes following the prescriptions by Chen et al. (2023; see also Cadelano et al. 2019). A selection of the evolutionary tracks is plotted in Figure 8. It can be clearly seen that the positions of the counterparts are compatible with those expected by the evolution of low-mass He WDs. To get a quantitative estimate of the companion physical properties (such as their masses, radii, cooling ages, surface gravities, and temperatures), we implemented the same approach described in detail in Cadelano et al. (2019; see also Cadelano et al. 2020a), by defining a logarithmic likelihood (see Equation (1) in Cadelano et al. 2020a) to quantify the probability of each point of each evolutionary track to reproduce the observed companion magnitudes in all the available filters. Then, for each of the investigated parameters, we obtained an estimate and its related uncertainty as the 0.16, 0.5, and 0.84 quantiles of the likelihood distributions. The derived properties of the three companions are listed in Table 4. Notably, all three companions are

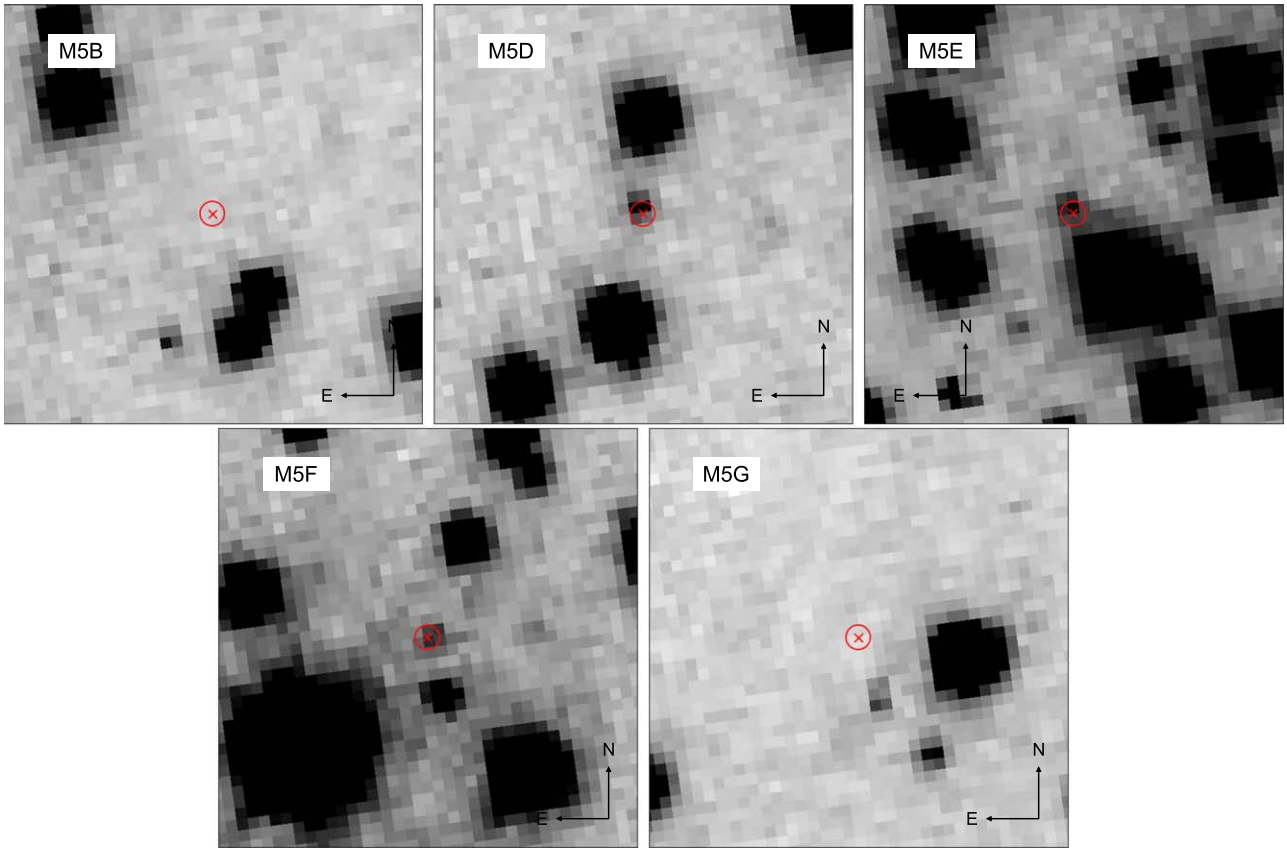

Figure 7. $1\farcs5 \times 1\farcs5$ finding charts of the regions surrounding the positions of M5B, M5D, M5E, M5F, and M5G in a combined F275W image. In each panel, the red cross indicates the pulsar position and the red circle has a radius of 3σ, using the combined optical and radio positional uncertainties.

extremely low mass WDs with similar masses, as commonly found for similar objects in other GCs.

The determination of the companion masses coupled with the binary orbital parameters (see Table 4) can be used to constrain the orbital inclination angles and, possibly, the NS masses. In fact, the masses of the binary components can be expressed as a function of the orbital parameters through the mass function. Figure 9 shows, for each of the three investigated systems, the companion mass as a function of the NS mass. Different curves correspond to different inclination angles, as predicted by the mass functions. In the case of M5D and M5F, it is most likely that the two binaries host a canonical NS. In fact, assuming a standard NS mass of 1.4 $M_{\odot}$, it can be seen that the derived companion masses imply that both systems are likely observed at very high inclination angles ($i \geqslant 80^{\circ}$), which is consistent with the detection of the Shapiro delay of M5F and, marginally, of M5D (Section 3.5). On the other hand, in the case of M5E, it is not possible to rule out the presence of a more massive NS. M5E could host a canonical NS and be observed at intermediate to high inclination angles ($45^{\circ} < i < 70^{\circ}$) or, alternatively, could host a more massive NS at high inclination angles.

3.9. X-Ray Counterparts to MSPs

We performed X-ray data reduction and analysis using CIAO[32] (Fruscione et al. 2006; v4.15.1 with CALDB 4.10.2). We first reprocessed the data set to create a new level = 2 event file and a new bad pixel file using `chandra_repro` script. We performed source detection in the 0.3–8 keV image using the `wavdetect` script,[33] with a scale list of [1, 1.4, 2, 4, 8] and a significance threshold of 10^{-6}. Four X-ray sources were detected in the vicinities of MSPs C, D, E, and G, respectively (Table 5), while no X-ray sources were detected around the timing positions of MSPs A, B, and F (see the zoom-in images in Figure 1). Therefore, for the counterparts to MSPs C, D, E, and G, we were able to extract their X-ray spectra and conduct rigorous spectral analysis. We note that we reanalyzed the X-ray spectrum of M5C to keep consistency in this work, though it has been presented in Zhao & Heinke (2022).

We applied `specextract` script to extract their spectra in 1″-radius regions centered at the corresponding X-ray positions (see Table 5), while the background spectra were extracted from nearby source-free regions. We then used the spectral analysis software BXA (Buchner et al. 2014), which connects the nested sampling algorithm UltraNest (Buchner 2021) with SHERPA,[34] to conduct Bayesian parameter estimation and model comparison. We fitted their spectra with three absorbed spectral models, blackbody (BB), NS hydrogen atmosphere (NSA; Heinke et al. 2006), and power law (PL), realized by `xsbbodyrad`, `xsnsatmos`, and `xspegpwrlw`, respectively, in SHERPA, which are commonly observed spectra from MSPs (see, e.g., Zhao & Heinke 2022). The interstellar

[32] Chandra Interactive Analysis of Observations, available at https://cxc.harvard.edu/ciao/.

[33] https://cxc.cfa.harvard.edu/ciao/threads/wavdetect/

[34] CIAO's modeling and fitting package, available at https://cxc.cfa.harvard.edu/sherpa/.

Table 3
Magnitudes and Magnitude Upper Limits Measured in Each Available Filter for the Five Investigated MSPs

Name	F275W	F336W	F390W	F435W	F606W	F814W
COM-M5B	>24.87	>25.24	>25.85	>25.98	>25.43	>23.48
COM-M5D	22.97 ± 0.05	23.10 ± 0.09	23.70 ± 0.02	23.59 ± 0.03	23.57 ± 0.02	23.08 ± 0.20
COM-M5E	23.24 ± 0.12	23.21 ± 0.14	23.95 ± 0.05	23.92 ± 0.10	...	...
COM-M5F	23.58 ± 0.11	23.46 ± 0.12	23.82 ± 0.05	24.35 ± 0.06	23.85 ± 0.08	23.4 ± 0.20
COM-M5G	>24.41	>24.11	>25.13	>25.18	>25.35	>25.01

Note. The companion star to M5E is heavily contaminated by nearby bright stars in the F606W and F814W; thus, no magnitudes or upper limits can be derived.

absorption toward M5 was modeled by the `xstbabs` model, with *wilm* abundances (Wilms et al. 2000) and *vern* photoionization cross sections (Verner et al. 1996), while the hydrogen column density ($N_{\rm H}$) was assumed to be fixed at 2.61×10^{20} cm^{-2}. This $N_{\rm H}$ was estimated using the correlation between $N_{\rm H}$ and optical extinction (A_V) in Bahramian et al. (2015), while the A_V toward M5 was calculated as $A_V = 3.1 \times E(B-V)$ (Cardelli et al. 1989), where $E(B-V) = 0.03$ is the foreground reddening toward M5 (Harris 2010).

To generate Bayesian parameter estimation, we defined uniform priors for the PL photon index (Γ) between 0 and 5, for NSA $\log_{10} T_{\rm eff}$ between 5 and 6.5, and a log-uniform prior for BB $kT_{\rm BB}$ between 10^{-4} and 10, where $T_{\rm eff}$ is the unredshifted effective temperature in kelvins and $kT_{\rm BB}$ is the BB temperature in keV. In addition, for the NSA model, the NS mass and radius were set to be $1.4\,M_\odot$ and 10 km, respectively, and the distance to M5 was assumed to be 7.5 kpc (Harris 2010). All priors for normalization parameters were defined to be log-uniform between 10^{-8} and 10^{2}. Note that the normalization parameters of BB and NSA models can be used to infer the effective surface emitting regions ($R_{\rm eff}$), whereas the normalization of the PL model directly returns the X-ray flux in a given band. Each X-ray spectrum was grouped to at least one photon per bin and filtered to a 0.3–8 keV range in the fitting process. We used the difference of log Bayesian evidence (Z) from the fitting results to compare models, where we adopted a difference of $\Delta \log_{10} Z > 1.5$ to rule out models (i.e., Jeffreys's scale; see Jeffreys 1939).

We present the spectral fitting results and X-ray properties of the four X-ray counterparts in Table 6. We found that all spectral models returned acceptable fits, with the NSA model having the largest likelihoods, whereas we were not able to rule out any spectral models by simply comparing the Bayesian evidence. On the other hand, the photon indices obtained from the PL model were all greater than ~2.5, implying substantial soft, thermal X-ray emission from these sources, which favors blackbody-like spectral models, BB and NSA. Moreover, the best-fit BB and NSA parameters are similar to those typically observed from MSPs in GCs (e.g., Bogdanov et al. 2006). It is also noticeable that the NSA model returned a likelihood about 10 times larger than the BB model in each of the four spectral fittings, suggesting that the NSA model better represents the thermal emission from MSPs, though both models are acceptable. Additionally, we examined combined models, such as PL+BB and PL+NSA, in spectral fittings, but these combined models did not improve fits significantly, and the parameters were more poorly constrained. Hence, based on the X-ray spectral fits and properties, we identified X-ray counterparts to four MSPs in M5 (including three newly identified counterparts to MSPs D, E, and G, respectively), whose spectra are well fitted by an absorbed NSA model with X-ray luminosities between 6.0×10^{30} erg s^{-1} and 1.2×10^{31} erg s^{-1}. We note that these X-ray luminosities are consistent with those typically observed for MSPs in GCs (see, e.g., Zhao & Heinke 2022). However, sources in M5 with X-ray luminosities lower than $\sim 5 \times 10^{30}$ erg s^{-1} (Bahramian et al. 2020) are undetectable owing to the long distance to this cluster and the limited exposure time (e.g., likely cases for MSPs A, B, and F).

Due to the lack of source detections around MSPs A, B, and F, we were unable to perform stringent spectral analysis for them. Nonetheless, to constrain their X-ray luminosities, we extracted the spectra from 1.″5-radius regions centered at the timing positions of MSPs A, B, and F, respectively, which took into account possible radio and X-ray positional offsets. We then simply fitted their spectra with an absorbed PL model with a photon index fixed to 2. The choice of $\Gamma = 2$ can include both thermal and nonthermal emission from an MSP and therefore reduce bias of model selection (Bogdanov et al. 2021). We also fitted their spectra with an absorbed NSA model by fixing $\log_{10} T_{\rm eff} = 6$, which is the average of the four best-fit NSA parameters of MSPs C, D, E, and G. The fitting results of MSPs A, B, and F are also presented in Table 6. We found that the X-ray luminosities fitted by PL models are lower than $\sim 7 \times 10^{30}$ erg s^{-1}, while the luminosities obtained from NSA models are lower than $\sim 3.5 \times 10^{30}$ erg s^{-1}. The difference in X-ray luminosities between the PL and NSA models is due to their different modeling of fluxes in the hard X-ray band, where nominal thermal X-rays are not expected. Considering that the limiting X-ray luminosity of a source to be detected in M5 is about 5×10^{30} erg s^{-1} (Bahramian et al. 2020), the upper limits set by PL models are very conservative.

4. Discussion

4.1. Properties of Pulsars in M5

Previous to this study, we already knew that the pulsar population in M5 consists of fast-spinning pulsars (with the slowest object having a spin period of ~8 ms) and is clearly dominated by binary systems: of the six previously known pulsars, five were in binaries, with a single isolated object, M5A. All the binaries have low-mass companions. All of this is still true after our new binary discovery, M5G.

Our timing solutions provide precise positions for the pulsars. All of them are located within 1.′2 (2.8 core radii) of the center of the GC, which is significantly smaller than the half-light and tidal radii (~1.′8 and ~24′, respectively; Harris 2010) that characterize the overall stellar distribution. This distribution is strongly reminiscent of that of 47 Tuc (Heinke et al. 2005), which is the result of mass segregation (with the NSs, being more massive, migrating to the center of the GC via

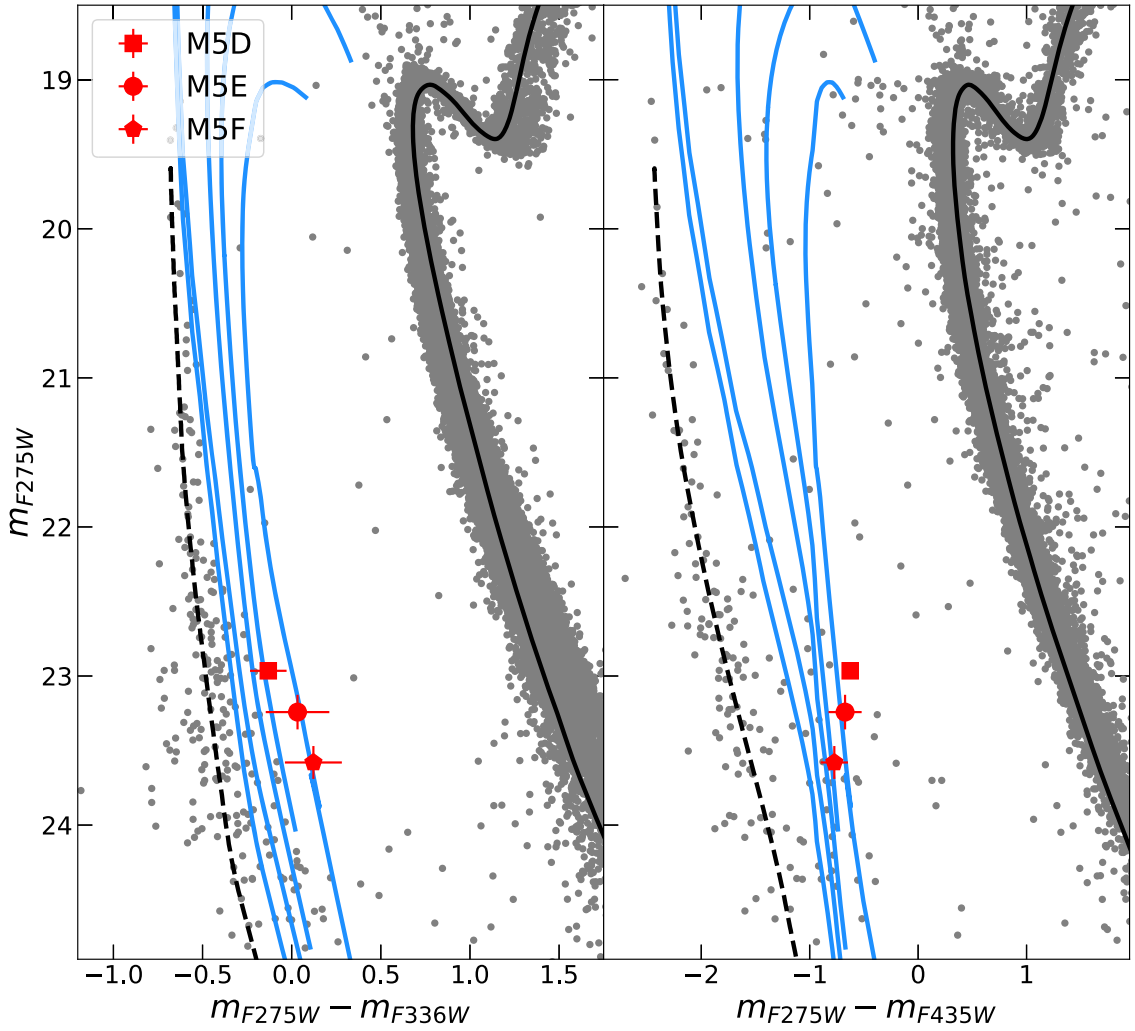

Figure 8. Left panel: CMD of M5 in a combination of the F275W and F336W filters. The red square, circle, and pentagon are the positions of the counterparts to M5D, M5E, and M5F, respectively. The solid and dashed black curves are a 12.5 Gyr stellar population isochrone and a 0.55 $M_{\odot}$ WD cooling track, respectively. Blue curves are cooling tracks of He WDs with masses of 0.17, 0.19, 0.21, 0.25, and 0.30 $M_{\odot}$, with increasing masses from left to right. Right panel: same as the left panel, but with a combination of F275W and F435W filters.

Table 4
Derived Properties of the Companions to M5D, M5E, and M5F

Parameter	M5D	M5E	M5F
Companion mass, m_c ($M_{\odot}$)	0.19 ± 0.02	0.19 ± 0.03	0.18 ± 0.03
Surface gravity, log g (cm s^{-2})	6.4 ± 0.3	6.5 ± 0.3	6.3 ± 0.3
Companion radius, R_c ($R_{\odot}$)	0.044 ± 0.01	0.042 ± 0.01	0.051 ± 0.015
Effective temperature, $T_{\rm eff}$ (K)	10400^{+1400}_{-800}	10000^{+1300}_{-1000}	8800^{+1100}_{-1000}
Cooling age (Gyr)	2.3 ± 1.0	2.8 ± 1.4	$1.8^{+2.0}_{-0.5}$

Note. Companion masses are from optical analysis.

dynamical friction) followed by an equilibrium, or "dynamical relaxation." This is typical of stellar populations with ages larger than the dynamical relaxation time, ∼0.2 Gyr for the core of M5 and ∼2.6 Gyr for the average star in the cluster (Harris 2010).

Our timing results revealed weak surface magnetic fields (smaller than 6×10^8 G) and advanced characteristic ages (gigayears; Table 2) for all seven pulsars in M5. For M5B, this can be additionally verified by its $\dot{P}_b$. Another important indication about the nature of these systems are the low eccentricities of all the newly discovered binaries. The large eccentricity of M5B marks it as the only binary pulsar in M5 that has had substantial orbital perturbations by close stellar encounters. This is more likely for wider systems, which present a larger cross section for such perturbations, and indeed M5B is precisely the binary with the largest orbital period.

The precise positions determined from timing allowed optical detections of the companions of M5D, M5E, and M5F (and, in an earlier work, of M5C). The colors and magnitudes of the companions point to a similar conclusion: they are very likely low-mass He WDs such as one would expect to find in low-eccentricity systems with fast MSPs. Their cooling ages are, again, of the order of a few gigayears.

Through the Chandra X-ray study of M5 MSPs, X-ray counterparts to four (MSPs C, D, E, and G) out of seven MSPs are identified, with new identifications of X-ray counterparts to MSPs D, E, and G, respectively. Thermal X-ray emission is observed from those four X-ray counterparts, whose spectra are well described by an absorbed NS hydrogen atmosphere model. Their unabsorbed X-ray luminosities (0.5–10 keV) are between

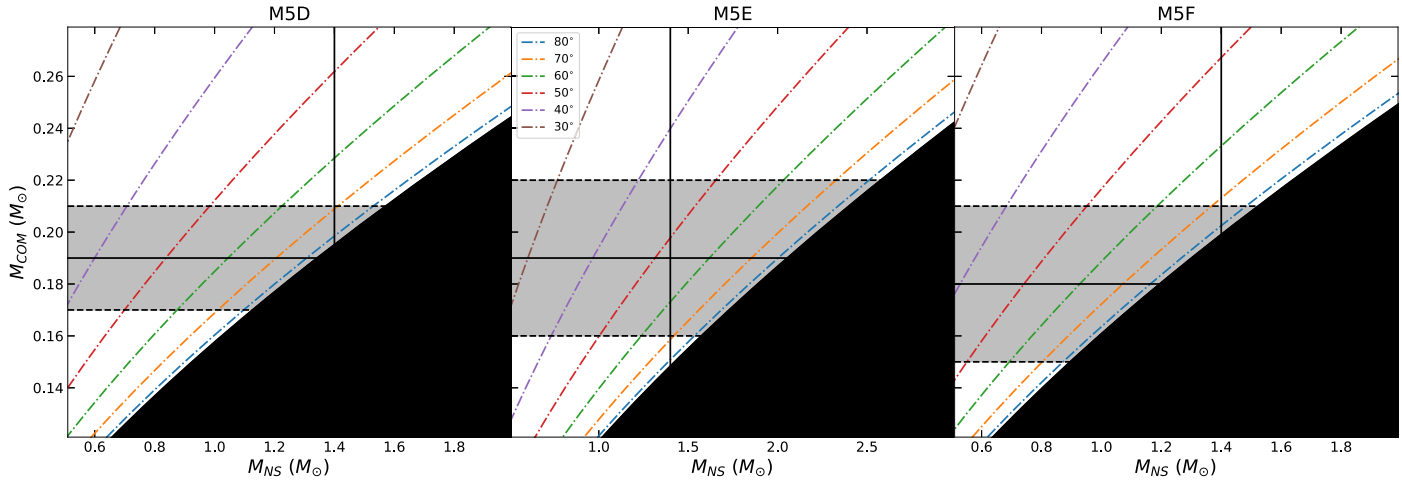

Figure 9. The mass of the NS as a function of companion mass for M5D, M5E, and M5F. The derived mass of the companion star is marked with a horizontal solid line, and the corresponding uncertainty is limited by two horizontal dashed lines in shallow areas. The colored curves represent the relationship between the companion masses and the NS masses at different inclinations, and the black region is excluded by the pulsar mass function.

Table 5
X-Ray Counterparts to Four MSPs

MSP Name	X-Ray Position[a] (hh:mm:ss.ss+dd:mm:ss.s)	PU[b] (arcseconds)	Offset[c] (arcseconds)
C	15:18:32.81 +02:04:47.5	0.52	0.40
D	15:18:30.40 +02:05:00.2	0.68	0.76
E	15:18:33.27 +02:04:37.4	0.37	0.78
G	15:18:28.73 +02:05:15.1	0.86	0.35

Notes. X-ray detections of four MSP counterparts using `wavdetect`.
[a] The X-ray centroids reported by `wavdetect`.
[b] X-ray positional uncertainties at a 95% confidence level, computed using Equation (12) in Kim et al. (2007).
[c] Angular offsets between timing and X-ray positions.

$\sim 6 \times 10^{30}$ erg s^{-1} and $\sim 1 \times 10^{31}$ erg s^{-1}, which are in the range typically observed from thermally emitting GC MSPs (Zhao & Heinke 2022). The two black widows, MSPs C (eclipsing) and G (noneclipsing), show little or no nonthermal X-ray emission, likely indicating weak synchrotron radiation produced by intrabinary shocks from these two spider pulsars. On the other hand, the X-ray luminosities of MSPs A, B, and F, which have no identified X-ray counterparts, are constrained to be lower than $\sim 4 \times 10^{30}$ erg s^{-1}, while their X-ray counterparts could be detected in the future with deeper X-ray observations.

4.2. The Single–Binary Encounter Rate

In its broad parameters (predominance of binaries, fast spins, small B fields and large characteristic ages, low orbital eccentricities, small companion masses, and large cooling ages for a few of the He WD companions) the pulsar population of M5 is similar to the MSP population observed in the Galactic disk, as expected from the low γ of M5. Thus, once an LMXB forms, it evolves undisturbed to form these types of systems, as in the Galactic disk.

The study of pulsars in low-γ GCs like M5 provides an important test of the scenario presented by Verbunt & Freire (2014). If the apparently high-B pulsars in some GCs were being produced in large numbers by a process other than LMXB disruption (for a summary of some of these processes, see Section 1 and, e.g., Boyles et al. 2011), then there should be no reason why they cannot be produced in a low-γ GC like M5. These alternative processes, like capture by a giant star and subsequent recycling, are, like the formation of low-B-field MSPs, proportional to Γ. Therefore, the lack of high-B-field pulsars relative to low-B-field pulsars in low-γ clusters like M5 —to which we add in this paper—adds to the evidence that the high-B-field pulsars form in a process that depends on γ, like LMXB disruption. It is important to continue searching for high-B-field pulsars in low-γ clusters; finding them might indicate alternative or additional formation channels for that type of pulsar.

4.3. The Cluster Dynamics

The formation of MSPs is a combined effect of NS evolution and the cluster dynamics. NSs were formed in the early stages of the GC because their progenitor massive stars have short lifetimes. A large fraction of NSs might escape from the GC owing to high-velocity kicks after asymmetric supernovae. Over billions of years, the remaining NSs in the GC core experience almost all of the GC's dynamical evolution, including two-body relaxation-driven mass segregation, core-collapse event(s), and the tidal dynamics between the GC and the Milky Way. All these mechanisms alter the density profile of GCs. The mass segregation leads to the central concentration of NSs, which then suffer less tidal effects from the Galaxy. The core collapse makes an ultradense core and leads to higher stellar encounter rates that can form pulsars, while the tidal dissolution stretches the cluster and strips stars away, regulating the stellar interaction rate.

The situation becomes more complex when considering the presence of a black hole (BH) population. Due to their significantly higher mass compared to NSs and normal stars, BHs tend to occupy the core region of the cluster until many of them are ejected through few-body interactions involving binary BHs and third bodies. As a result, the observed central surface density appears to be low, lacking the characteristic feature of core collapse (e.g., Breen & Heggie 2013). The existence of BHs might also reduce the stellar interaction rate between NSs and stars (Ye et al. 2019). Instead, NSs might interact with binary BHs and escape from the cluster core.

Table 6
X-Ray Spectral Fitting Results of M5 MSPs

MSP Name	Spectral Model[a]	Parameter[b]	$R_{\rm eff}$[c] (km)	$F_{0.5-2}$[d] (10^{-16} erg cm^{-2} s^{-1})	F_{2-8}[d]	$L_{0.5-10}$[e] (10^{30} erg s^{-1})	$\log_{10}Z$[f]
A	PL	2	⋯	<4.6	<4.6	<6.6	⋯
	NSA	6	<1.1	<3.8	<0.1	<2.5	⋯
B	PL	2	⋯	<4.7	<5.5	<6.8	⋯
	NSA	6	<1.3	<4.8	<0.1	<3.2	⋯
C	BB	$0.13^{+0.03}_{-0.02}$	$0.62^{+0.41}_{-0.27}$	$10.0^{+4.0}_{-2.9}$	$0.0^{+0.0}_{-0.0}$	$6.7^{+2.7}_{-2.0}$	−1.1
	NSA	$5.80^{+0.16}_{-0.16}$	$6.00^{+11.25}_{-3.66}$	$9.7^{+3.7}_{-3.0}$	$0.0^{+0.1}_{-0.0}$	$6.5^{+2.6}_{-2.0}$	0
	PL	$3.84^{+0.74}_{-0.70}$	⋯	$8.6^{+3.4}_{-2.5}$	$0.7^{+1.3}_{-0.5}$	$6.3^{+3.0}_{-2.0}$	−0.3
D	BB	$0.14^{+0.04}_{-0.03}$	$0.54^{+0.49}_{-0.25}$	$9.4^{+4.4}_{-2.9}$	$0.0^{+0.0}_{-0.0}$	$6.3^{+3.0}_{-2.0}$	−0.7
	NSA	$5.83^{+0.18}_{-0.17}$	$4.83^{+9.66}_{-3.18}$	$8.8^{+4.0}_{-2.9}$	$0.0^{+0.1}_{-0.0}$	$6.0^{+2.8}_{-2.0}$	0
	PL	$3.65^{+0.79}_{-0.80}$	⋯	$8.3^{+3.5}_{-2.8}$	$0.9^{+2.1}_{-0.6}$	$6.4^{+3.3}_{-2.4}$	−0.4
E	BB	$0.27^{+0.06}_{-0.05}$	$0.14^{+0.07}_{-0.05}$	$16.1^{+3.5}_{-3.3}$	$1.3^{+1.7}_{-0.9}$	$11.9^{+2.9}_{-2.5}$	−0.9
	NSA	$6.29^{+0.11}_{-0.12}$	$0.50^{+0.40}_{-0.20}$	$15.8^{+4.1}_{-3.4}$	$1.7^{+1.6}_{-0.9}$	$11.9^{+3.2}_{-2.8}$	0
	PL	$2.39^{+0.44}_{-0.42}$	⋯	$13.9^{+3.6}_{-2.9}$	$8.2^{+6.7}_{-4.1}$	$15.9^{+6.5}_{-4.3}$	−0.5
F	PL	2	⋯	<2.4	<2.4	<3.4	⋯
	NSA	6	<0.9	<2.3	<0.1	<1.6	⋯
G	BB	$0.23^{+0.08}_{-0.05}$	$0.15^{+0.13}_{-0.07}$	$8.7^{+3.9}_{-2.8}$	$0.3^{+0.9}_{-0.2}$	$6.3^{+2.9}_{-2.2}$	−1.0
	NSA	$6.15^{+0.18}_{-0.18}$	$0.75^{+1.32}_{-0.44}$	$8.8^{+3.5}_{-3.0}$	$0.4^{+0.9}_{-0.3}$	$6.2^{+2.7}_{-2.1}$	0
	PL	$2.75^{+0.77}_{-0.65}$	⋯	$8.1^{+2.9}_{-2.6}$	$2.7^{+4.7}_{-1.9}$	$7.7^{+5.0}_{-2.9}$	−0.2

Notes. Due to the lack of detections of X-ray counterparts to MSPs A, B, and F, their spectra were only fitted with an absorbed power-law model by fixing $\Gamma = 2$ and an absorbed NSA model by fixing $\log_{10} T_{\rm eff} = 6$. The fitting results are presented as 1σ upper limits. $N_{\rm H}$ toward M5 was fixed at 2.61×10^{20} cm^{-2} for all the fits. The quoted uncertainties represent 1σ confidence level.

[a] X-ray spectral models applied in this work. BB: blackbody; NSA: NS hydrogen atmosphere (Heinke et al. 2006); PL: power law.

[b] The best-fit $kT_{\rm BB}$ (in keV), $\log_{10} T_{\rm eff}$ (in $\log_{10}$ kelvin), and Γ of BB, NSA, and PL models, respectively.

[c] Effective source-emitting region, calculated assuming a distance to M5 of 7.5 kpc.

[d] Unabsorbed fluxes in 0.5–2 keV and 2–8 keV energy bands, respectively, in units of 10^{-16} erg cm^{-2} s^{-1}.

[e] Unabsorbed X-ray luminosities in 0.5–10 keV band, in units of 10^{30} erg s^{-1}.

[f] Log Bayesian evidence of fittings, normalized to the highest evidence in each case (i.e., 0 represents the model with highest likelihood).

For the case of M5, no clear evidence has been found from its density profile (see, e.g., the GC parameter catalogs of Harris 1996; Miocchi et al. 2013; Baumgardt & Hilker 2018)[35,36] or its distribution of blue straggler stars that the cluster has experienced core-collapse event(s) (see the review paper Ferraro et al. 2020, for using blue straggler stars as a "dynamical clock" to date the time of core collapse). Thus, it is not expected that the inner-cluster dynamics can result in very high stellar encounter rates to form MSPs.

However, M5 is known to have at least one stellar tidal stream (see, e.g., Mateu 2023), which provides evidence of significant mass loss due to tidal interactions with the gravitational potential of the Milky Way. The trailing tidal tail of M5 spans an extensive portion of the sky, covering ∼50° (Grillmair 2019). This suggests that M5 has lost a lot of mass at its outer boundary and should have been much heavier in its early life than it appears now. Given its likely origin as an accreted GC from outside the Milky Way (Massari et al. 2019), M5 has a highly eccentric orbit ($e > 0.8$; see, e.g., Vasiliev & Baumgardt 2021), with its orbital perigalacticon very close to the Galactic center.[37] Consequently, the strong tidal forces near the Galactic center, particularly the tidal shocks, are likely responsible for the significant loss of stars that occurs each time the cluster passes the perigalacticon (see also discussions in Grillmair 2019). This mass loss affects not only the outer region of the cluster but also the cluster core region. Indeed, based on HST data and *N*-body simulation, Baumgardt & Hilker (2018) have determined that the current mass of M5 is $3.72 \times 10^5 M_\odot$, with a half-mass radius (r_h) of 5.58 pc. However, M5 exhibits a relatively low central density (4.68×10^3 $M_\odot$ pc^{-3}) and central escape velocity (30.4 km s^{-1}). While its half-mass radius is typical for a cluster of its mass and Galactocentric radius, the lower central density and central escape velocity of M5 suggest that its core has undergone significant stellar depletion, including the loss of NSs.

By neglecting the evolution of the Milky Way potential, we can estimate the dissolution time (t_d) of M5, which represents the member star dispersion timescale of the cluster, using the formula derived by Baumgardt & Makino (2003) and Wang (2020),

$$t_d \sim t_{\rm rh}^{3/4} t_{\rm cr}^{1/4} (r_t/r_h)^{3/2} (1 - e), \quad (5)$$

where $t_{\rm rh}$, $t_{\rm cr}$, r_t, and e are the half-mass relaxation time, crossing time, tidal radius, and eccentricity of the star cluster's orbit around the Galaxy, respectively.

For M5, the present-day values are approximately $t_{\rm rh} \approx 3.2$ Gyr, $t_{\rm cr} \approx 0.32$ Myr, and $r_t \approx 81$ pc according to Baumgardt & Hilker (2018). The corresponding dissolution time is $t_d \approx 4.3$ Gyr, i.e., the timescale over which the cluster disperses a significant portion of its member stars is shorter than the cluster age (∼11.5 Gyr; VandenBerg et al. 2013). Therefore, it can be inferred that M5 has experienced significant mass loss in the past. Moreover, considering the possibility of the existence of a BH population, the t_d of M5 might be even shorter (Wang

[35] https://people.smp.uq.edu.au/HolgerBaumgardt/globular/

[36] 2010 edition: https://physics.mcmaster.ca/~harris/mwgc.dat.

[37] See the orbit integration figure of M5 at https://people.smp.uq.edu.au/HolgerBaumgardt/globular/fits/ngc5904.html.

2020). We contend that, due to the significant mass loss experienced by M5, the potential ejection of NSs through few-body interactions within the core, and the initial natal kick imparted to NSs during supernova events, a substantial fraction of NSs, even MSPs, have been lost over the course of M5's history.

The present-day mass function of M5, as observed in Baumgardt & Sollima (2017), exhibits a power-law index of $\alpha \approx -0.85$ within the mass range of 0.2–0.8 $M_\odot$. Referring to the Kroupa (2001) initial mass function, which has an index of $\alpha \approx -1.3$, the higher α in M5 suggests that mass segregation may have occurred, leading to a preferential loss of low-mass stars through tidal evaporation. Therefore, we anticipate that the NS fraction on the tidal stream will be lower than that in the cluster.

The dynamical evolution of M5 discussed above shapes the cluster density profile and stellar mass function. Consequently, it also affects the NS population and the collision rate in the cluster. The remaining MSPs and their distribution are the selection effect resulting from the dynamical evolution that M5 has undergone.

5. Summary

We have carried out a comprehensive multiwavelength study of the relatively low mass, likely extragalactic-accreted, non-core-collapsed GC M5. We utilized data from Arecibo, FAST, HST, and Chandra. The main results are as follows:

1. With FAST, we discovered PSR J1518+0204G, the seventh pulsar in M5. M5G, which is in a black widow binary system, has a ∼2.75 ms spin period and 0.11 day orbital period.
2. All seven pulsars are fast MSPs with spin period $P <$ 8 ms. Five out of seven pulsars in M5 are in low-eccentricity binaries, with low-mass companions. The average orbital eccentricity of the M5 binary pulsars is $e = 0.024$. The general GC pulsar population has an average spin period $P = 18$ ms and an average eccentricity $e = 0.11$.
3. With data from both Arecibo and FAST, spanning 34 yr, we achieved new phase-connected timing solutions for M5D, M5E, M5F, and M5G and improved those for M5A, M5B, and M5C. These show that pulsars in M5 have relatively low B fields ($<6.2 \times 10^8$ G) and large (>0.8 Gyr) characteristic ages; they are likely similar to the MSP population in the Galactic disk.
4. The proper motions of five pulsars (M5A to E) measured in this work, with an average value of $\mu_\alpha = 4.14 \pm 0.14$ mas yr^{-1} and $\mu_\delta = -10.25 \pm 0.4$ mas yr^{-1}, are consistent with the Gaia EDR3 proper motion of the cluster. All five pulsars are consistent with the escape velocity circle on the μ_α–μ_δ plane.
5. We measured M5B's periastron advance rate as $\dot{\omega} = 0.^\circ01361(6)$. This represents an order-of-magnitude improvement over, while still within 1σ of, previous measurements, resulting in updated mass measurements: $m_c = 0.163^{+0.095}_{-0.020}\,M_\odot$, $m_p = 1.981^{+0.038}_{-0.088}\,M_\odot$ and $M_T = 2.157^{+0.028}_{-0.027}\,M_\odot$ for the companion, pulsar, and the total mass of the M5B system. M5B remains a likely heavy NS, with little constraint on its inclination, except that it cannot be close to being edge on.
6. We detected the Shapiro delay in M5F, and possibly in M5D, in radio timing data. M5F was determined to possess a high inclination (close to 89°), $m_c \sim 0.2\,M_\odot$ ($\sim\pm50\%$ uncertainty), and $m_p \sim 1.4\,M_\odot$. These values are consistent with those estimated based on optical data.
7. The companions of M5D, E and F are detected on archival HST images, which shows that they are low-mass He WDs with cooling ages of a few gigayears. These are consistent with the large characteristic ages inferred from timing.
8. Pulsars C, D, E, and G were also detected in Chandra data, from which X-ray spectra were newly extracted for M5D, M5E, and M5G and can be well fitted by absorbed NS hydrogen atmosphere models.
9. All characteristics of the pulsar population are consistent with the theoretical expectations for a low-γ GC. The apparent lack of high-B pulsars relative to the low-B pulsars in M5 and other low-γ clusters favors γ-dependent processes (such as LMXB disruption) for the formation of high-B-field pulsars in GCs, while disfavoring Γ-dependent ones (such as giant star capture).
10. The evolutionary history and status of M5 are influenced by significant mass loss through tidal interaction with the Milky Way, as evidenced by its relatively low mass ($3.72 \times 10^5\ M_\odot$), non-core-collapsed state and having at least one stellar tidal stream.

Acknowledgments

This work is supported by NSFC grant Nos. 11988101 and 11725313, by the National Key R&D Program of China No. 2017YFA0402600, by Key Research Project of Zhejiang Lab No. 2021PE0AC03, and by Chinese Academy of Sciences President's International Fellowship Initiative, grant No. 2023VMC0001. L.Z. is supported by ACAMAR Postdoctoral Fellowship and NSFC grant No. 12103069. A.R. gratefully acknowledges support by the Chinese Academy of Sciences President's International (PIFI) Fellowship Initiative, grant No. 2023VMC0001, and by the National Astronomical Observatory of China (NAOC). J.C. acknowledges support from the China Scholarship Council. M.C. and C.P. acknowledge financial support from the project Light-on-Dark granted by MIUR through PRIN2017-2017K7REXT. S.D. is the recipient of an Australian Research Council Discovery Early Career Award (DE210101738) funded by the Australian Government. X.F. acknowledges the support of NSFC grant No. 12203100 and the China Manned Space Project with No. CMS-CSST-2021-A08. C.H. is supported by NSERC Discovery Grant RGPIN-2016-04602. X.H. is supported by the NSFC grant No. 12041303. S.M.R. is a CIFAR Fellow and is supported by the NSF Physics Frontiers Center award 2020265. J.Z. is supported by a China Scholarship Council scholarship, No. 202108180023. The National Radio Astronomy Observatory is a facility of the National Science Foundation operated under cooperative agreement by Associated Universities, Inc., and also this work has been funded using resources from the INAF Large Grant 2022 "GCjewels" (P.I. Andrea Possenti) approved with the Presidential Decree 30/2022. Pulsar research at UBC is funded by an NSERC Discovery Grant and by the Canadian Institute for Advanced Research. We thank Ramesh Karuppusamy and Matthew Bailes for a careful reading of the manuscript and helpful suggestions.

The X-ray analysis in this paper employs a Chandra data set, obtained by the Chandra X-ray Observatory, contained at doi:10.25574/cdc.160.

ORCID iDs

Lei Zhang https://orcid.org/0000-0001-8539-4237
Paulo C. C. Freire https://orcid.org/0000-0003-1307-9435
Alessandro Ridolfi https://orcid.org/0000-0001-6762-2638
Craig O. Heinke https://orcid.org/0000-0003-3944-6109
Jianxing Chen https://orcid.org/0000-0002-8004-549X
Mario Cadelano https://orcid.org/0000-0002-5038-3914
Cristina Pallanca https://orcid.org/0000-0002-7104-2107
Xian Hou https://orcid.org/0000-0003-0933-6101
Shi Dai https://orcid.org/0000-0002-9618-2499
Guodong Li https://orcid.org/0000-0003-4007-5771
Scott M. Ransom https://orcid.org/0000-0001-5799-9714
Ingrid Stairs https://orcid.org/0000-0001-9784-8670
Pei Wang https://orcid.org/0000-0002-3386-7159
Long Wang https://orcid.org/0000-0001-8713-0366
Na Wang https://orcid.org/0000-0002-9786-8548
Weiwei Zhu https://orcid.org/0000-0001-5105-4058
Yongkun Zhang https://orcid.org/0000-0002-8744-3546
Di Li https://orcid.org/0000-0003-3010-7661

References

Abbate, F., Possenti, A., Ridolfi, A., et al. 2018, MNRAS, 481, 627
Andersen, B. C., & Ransom, S. M. 2018, ApJL, 863, L13
Anderson, S. B., Wolszczan, A., Kulkarni, S. R., & Prince, T. A. 1997, ApJ, 482, 870
Antoniadis, J., Freire, P. C. C., Wex, N., et al. 2013, Sci, 340, 448
Bahramian, A., Heinke, C. O., Degenaar, N., et al. 2015, MNRAS, 452, 3475
Bahramian, A., Strader, J., Miller-Jones, J. C. A., et al. 2020, ApJ, 901, 57
Baumgardt, H., & Hilker, M. 2018, MNRAS, 478, 1520
Baumgardt, H., & Makino, J. 2003, MNRAS, 340, 227
Baumgardt, H., & Sollima, S. 2017, MNRAS, 472, 744
Bhattacharya, D., & van den Heuvel, E. P. J. 1991, PhR, 203, 1
Bogdanov, S., Bahramian, A., Heinke, C. O., et al. 2021, ApJ, 912, 124
Bogdanov, S., Grindlay, J. E., Heinke, C. O., et al. 2006, ApJ, 646, 1104
Boyles, J., Lorimer, D. R., Turk, P. J., et al. 2011, ApJ, 742, 51
Breen, P. G., & Heggie, D. C. 2013, MNRAS, 432, 2779
Buchner, J. 2021, JOSS, 6, 3001
Buchner, J., Georgakakis, A., Nandra, K., et al. 2014, A&A, 564, A125
Cadelano, M., Chen, J., Pallanca, C., et al. 2020a, ApJ, 905, 63
Cadelano, M., Ferraro, F. R., Istrate, A. G., et al. 2019, ApJ, 875, 25
Cadelano, M., Saracino, S., Dalessandro, E., et al. 2020b, ApJ, 895, 54
Cardelli, J. A., Clayton, G. C., & Mathis, J. S. 1989, ApJ, 345, 245
Chen, J., Cadelano, M., Pallanca, C., et al. 2023, ApJ, 948, 84
Chen, J., Ferraro, F. R., Cadelano, M., et al. 2021, NatAs, 5, 1170
Clark, G. W. 1975, ApJL, 199, L143
Damour, T., & Deruelle, N. 1986, AIHPA, 44, 263
DeCesar, M. E., Ransom, S. M., Kaplan, D. L., Ray, P. S., & Geller, A. M. 2015, ApJL, 807, L23
Fabian, A. C., Pringle, J. E., & Rees, M. J. 1975, MNRAS, 172, 15
Ferraro, F. R., Lanzoni, B., & Dalessandro, E. 2020, RLSFN, 31, 19
Fonseca, E., Cromartie, H. T., Pennucci, T. T., et al. 2021, ApJL, 915, L12
Freire, P. C. C., Hessels, J. W. T., Nice, D. J., et al. 2005, ApJ, 621, 959
Freire, P. C. C., Ridolfi, A., Kramer, M., et al. 2017, MNRAS, 471, 857
Freire, P. C. C., & Wex, N. 2010, MNRAS, 409, 199
Freire, P. C. C., Wolszczan, A., van den Berg, M., & Hessels, J. W. T. 2008, ApJ, 679, 1433
Fruscione, A., McDowell, J. C., Allen, G. E., et al. 2006, Proc. SPIE, 6270, 62701V
Gaia Collaboration, Vallenari, A., Brown, A. G. A., et al. 2023, A&A, 674, A1
Gehrels, N. 1986, ApJ, 303, 336
Goldsbury, R., Richer, H. B., Anderson, J., et al. 2010, AJ, 140, 1830
Grillmair, C. J. 2019, ApJ, 884, 174
Harris, W. E. 1996, AJ, 112, 1487
Harris, W. E. 2010, arXiv:1012.3224
Heinke, C. O., Grindlay, J. E., Edmonds, P. D., et al. 2005, ApJ, 625, 796
Heinke, C. O., Rybicki, G. B., Narayan, R., & Grindlay, J. E. 2006, ApJ, 644, 1090
Hessels, J. W. T., Ransom, S. M., Stairs, I. H., Kaspi, V. M., & Freire, P. C. C. 2007, ApJ, 670, 363
Hidalgo, S. L., Pietrinferni, A., Cassisi, S., et al. 2018, ApJ, 856, 125
Hills, J. G. 1976, MNRAS, 175, 1P
Hobbs, G. B., Edwards, R. T., & Manchester, R. N. 2006, MNRAS, 369, 655
Hotan, A. W., van Straten, W., & Manchester, R. N. 2004, PASA, 21, 302
Istrate, A. G., Marchant, P., Tauris, T. M., et al. 2016, A&A, 595, A35
Istrate, A. G., Tauris, T. M., Langer, N., & Antoniadis, J. 2014, A&A, 571, L3
Jacoby, B. A., Cameron, P. B., Jenet, F. A., et al. 2006, ApJL, 644, L113
Jeffreys, H. 1939, Theory of Probability (Oxford: Oxford Univ. Press)
Kamann, S., Husser, T. O., Dreizler, S., et al. 2018, MNRAS, 473, 5591
Kim, M., Kim, D.-W., Wilkes, B. J., et al. 2007, ApJS, 169, 401
King, I. 1962, AJ, 67, 471
Kroupa, P. 2001, MNRAS, 322, 231
Lange, C., Camilo, F., Wex, N., et al. 2001, MNRAS, 326, 274
Lanzoni, B., Ferraro, F. R., Mucciarelli, A., et al. 2018, ApJ, 861, 16
Li, D., Wang, P., Qian, L., et al. 2018, IMMag, 19, 112
Lyne, A. G., Brinklow, A., Middleditch, J., Kulkarni, S. R., & Backer, D. C. 1987, Natur, 328, 399
Massari, D., Koppelman, H. H., & Helmi, A. 2019, A&A, 630, L4
Mateu, C. 2023, MNRAS, 520, 5225
McMillan, P. J. 2017, MNRAS, 465, 76
Miocchi, P., Lanzoni, B., Ferraro, F. R., et al. 2013, ApJ, 774, 151
Mott, A. J., & Freire, P. C. 2003, AAS Meeting, 203, 53.07
Nan, R., Li, D., Jin, C., et al. 2011, IJMPD, 20, 989
Ng, C., Champion, D. J., Bailes, M., et al. 2015, MNRAS, 450, 2922
O'Donnell, J. E. 1994, ApJ, 422, 158
Pallanca, C., Ransom, S. M., Ferraro, F. R., et al. 2014, ApJ, 795, 29
Pan, Z., Qian, L., Ma, X., et al. 2021, ApJL, 915, L28
Park, R. S., Folkner, W. M., Williams, J. G., & Boggs, D. H. 2021, AJ, 161, 105
Phinney, E. S. 1993, in ASP Conf. Ser. 50, Structure and Dynamics of Globular Clusters, ed. S. G. Djorgovski & G. Meylan (San Francisco, CA: ASP), 141
Pietrinferni, A., Hidalgo, S., Cassisi, S., et al. 2021, ApJ, 908, 102
Prager, B. J., Ransom, S. M., Freire, P. C. C., et al. 2017, ApJ, 845, 148
Ransom, S. M., Eikenberry, S. S., & Middleditch, J. 2002, AJ, 124, 1788
Ridolfi, A., Freire, P. C. C., Gautam, T., et al. 2022, A&A, 664, A27
Ridolfi, A., Freire, P. C. C., Torne, P., et al. 2016, MNRAS, 462, 2918
Salaris, M., Cassisi, S., Pietrinferni, A., & Hidalgo, S. 2022, MNRAS, 509, 5197
Shapiro, I. I. 1964, PhRvL, 13, 789
Shklovskii, I. S. 1970, SvA, 13, 562
Splaver, E. M., Nice, D. J., Arzoumanian, Z., et al. 2002, ApJ, 581, 509
Stetson, P. B. 1987, PASP, 99, 191
Stetson, P. B. 1994, PASP, 106, 250
Sutantyo, W. 1975, A&A, 44, 227
Tauris, T. M., & Savonije, G. J. 1999, A&A, 350, 928
van Straten, W., & Bailes, M. 2011, PASA, 28, 1
VandenBerg, D. A., Brogaard, K., Leaman, R., & Casagrande, L. 2013, ApJ, 775, 134
Vasiliev, E., & Baumgardt, H. 2021, MNRAS, 505, 5978
Verbunt, F., & Freire, P. C. C. 2014, A&A, 561, A11
Verbunt, F., & Hut, P. 1987, in IAU Symp. 125, The Origin and Evolution of Neutron Stars, ed. D. J. Helfand & J. H. Huang (Dordrecht: D. Reidel), 187
Verner, D. A., Ferland, G. J., Korista, K. T., & Yakovlev, D. G. 1996, ApJ, 465, 487
Wang, L. 2020, MNRAS, 491, 2413
Wilms, J., Allen, A., & McCray, R. 2000, ApJ, 542, 914
Ye, C. S., Kremer, K., Chatterjee, S., Rodriguez, C. L., & Rasio, F. A. 2019, ApJ, 877, 122
Zhang, L., Hobbs, G., Li, D., et al. 2016, RAA, 16, 151
Zhao, J., & Heinke, C. O. 2022, MNRAS, 511, 5964